



**BOUNDARY LAYER CONTROL OF A
CIRCULAR CYLINDER USING A
SYNTHETIC JET**

THESIS

Christopher K. Smith, Captain, USAF

AFIT/GAE/ENY/05-J12

**DEPARTMENT OF THE AIR FORCE
AIR UNIVERSITY**

AIR FORCE INSTITUTE OF TECHNOLOGY

Wright-Patterson Air Force Base, Ohio

APPROVED FOR PUBLIC RELEASE; DISTRIBUTION UNLIMITED.

The views expressed in this thesis are those of the author and do not reflect the official policy or position of the United States Air Force, Department of Defense, or the United States Government.

AFIT/GAE/ENY/05-J12

BOUNDARY LAYER CONTROL OF A CIRCULAR CYLINDER USING A
SYNTHETIC JET

THESIS

Presented to the Faculty

Department of Aeronautics and Astronautics

Graduate School of Engineering and Management

Air Force Institute of Technology

Air University

Air Education and Training Command

In Partial Fulfillment of the Requirements for the
Degree of Master of Science in Aeronautical Engineering

Christopher K. Smith, BSE

Captain, USAF

June 2005

APPROVED FOR PUBLIC RELEASE; DISTRIBUTION UNLIMITED.

AFIT/GAE/ENY/05-J12

BOUNDARY LAYER CONTROL OF A CIRCULAR CYLINDER USING A
SYNTHETIC JET

Christopher K. Smith, BSE
Captain, USAF

Approved:

Dr. Milton E. Franke (Chairman)

date

Dr. Richard Cobb (Member)

date

Dr. Mark Reeder (Member)

date

Abstract

Active control of flow around a circular cylinder at a sub-critical Reynolds number was studied experimentally. The flow was controlled by using a synthetic jet which ran span wise along the cylinder and emanated radially from the cylinder. The experiments were conducted over a two dimensional cylinder in a water tunnel at a Reynolds number of approximately 5800. Seven different jet locations and seven different jet oscillation frequencies were examined. Particle image velocimetry (PIV) was used for flow visualization. The synthetic jet proved to delay flow separation at a wide range of locations and oscillation frequencies. The greatest positive effect on the boundary layer was determined to be when the jet was placed at an angle of 70° to the on coming flow at an oscillatory momentum blowing coefficient at 1.03, and non-dimensional frequency of 0.9. Boundary layer separation was delayed from approximately 90° to approximately 140° and the momentum deficit was reduced by 77-88%.

Acknowledgments

I would like to thank my thesis advisor Dr. Franke for allowing me to continue my studies at AFIT. I would also like to thank Dr. Reeder for his insights and suggestion during the course of the research. I am grateful to Dwight Gehring who helped me set up the experiment and Mr. LeValley and Mr. Jarusiewicz for turning my rough drawing into a working contraption.

Most of all I would like to thank my family. If it was not for your support and never ending belief in me I doubt that I would have made it through this program. Lastly, I would like to thank my best friend during my thesis research, caffeine. Whether you were coffee or diet soda, you kept me company on the long nights taking data and writing this report.

Christopher K. Smith

TABLE OF CONTENTS

| | Page |
|--|------|
| Abstract..... | iv |
| Acknowledgments..... | v |
| List of Figures..... | viii |
| List of Tables..... | xi |
| List of symbols..... | xii |
| Chapter 1. Introduction..... | 1 |
| 1.1 Background..... | 2 |
| 1.2 Objective..... | 4 |
| 1.3 Organization..... | 5 |
| Chapter 2. Theory | 6 |
| 2.1 Cylinder Boundary Layer and Wake..... | 6 |
| 2.2 Synthetic Jet Theory | 11 |
| 2.2.1 Synthetic Jet in Cross Flow | 13 |
| 2.3 Particle Image Velocimetry..... | 14 |
| 2.4 Scotch-Yoke Theory | 16 |
| Chapter 3. Experimental Setup and Procedure..... | 18 |
| 3.1 Water Tunnel..... | 18 |
| 3.2 Synthetic Jet Components..... | 20 |
| 3.2.1 Cylinders..... | 20 |
| 3.2.2 Piston, Cylinder, and Scotch-Yoke Mechanism..... | 23 |
| 3.2.3 Stepper Motor | 24 |
| 3.3 Particle Image Velocimetry..... | 26 |
| 3.3.1 Laser and Light Arm..... | 26 |
| 3.3.2 Seeding Particles..... | 27 |
| 3.3.3 Video Capture | 27 |
| 3.3.4 Image Processing | 28 |
| 3.4 Experimental Procedure..... | 29 |

| | Page |
|---|------|
| 3.4.1 Data Collection Procedure | 29 |
| 3.4.2 Test points | 30 |
| Chapter 4. Results..... | 32 |
| 4.1 Determining the Free Stream Flow Velocity | 32 |
| 4.2 Synthetic Jet Characteristics | 34 |
| 4.3 Synthetic Jet Effect on Boundary Layer | 38 |
| 4.4 Synthetic Jet Control Mechanisms | 54 |
| 4.4.1 Case 1 Control Mechanism..... | 54 |
| 4.4.2 Case 2 and Case 3 Control Mechanism | 57 |
| 4.5 Synthetic Jet Effect on Wake of Cylinder..... | 58 |
| Chapter 5. Conclusions and Recommendations | 63 |
| 5.1 Conclusions..... | 63 |
| 5.2 Recommendations..... | 63 |
| Appendix A. Streamline Velocity Figures | 65 |
| Appendix B. Matlab Code used to determine Synthetic Jet Parameters and Sample Calculations | 69 |
| Appendix C. Velocity Profiles | 74 |
| Bibliography..... | 79 |
| Vita..... | 81 |

List of Figures

| | Page |
|--|------|
| Figure 1 Boundary Layer Separation on a Cylinder (4) | 8 |
| Figure 2 Close-up View Boundary Layer Separation on a Cylinder (8) | 8 |
| Figure 3 Progression of the Wake Behind a Cylinder (12) | 9 |
| Figure 4 Strouhal Number versus Reynolds Number for Flow Around a Cylinder (18) .. | 11 |
| Figure 5 Typical PIV Setup (5) | 16 |
| Figure 6 Water Tunnel and Experimental Setup | 19 |
| Figure 7 Motor Frequencies versus Water Tunnel Speed (17)..... | 20 |
| Figure 8 Baseline Cylinder (Left) Synthetic Jet Cylinder (Right)..... | 22 |
| Figure 9 Synthetic Jet Cylinder | 22 |
| Figure 10 Synthetic Jet Cylinder Mounted in the Test Section | 23 |
| Figure 11 Scotch-Yoke Mechanism, Piston, and Cylinder..... | 24 |
| Figure 12 Stepper Motor..... | 26 |
| Figure 13 Laser and Light Arm | 27 |
| Figure 14 Redlake Camera | 28 |
| Figure 15 Location of Angular Positions of Synthetic Jet..... | 31 |
| Figure 16 PIV Velocity Measurement vs. Tunnel Speed Setting..... | 33 |
| Figure 17 Average Velocity of Jet Operating at 2.5 Hz | 35 |
| Figure 18 Synthetic Jet During Ejection at Operating 2.5 Hz | 36 |
| Figure 19 Synthetic Jet Post Ejection Operating at 2.5 Hz..... | 37 |
| Figure 20 Synthetic Jet During Suction Operating at 2.5 Hz | 37 |
| Figure 21 Laser Light Refraction | 38 |
| Figure 22 Streamline Velocity Plot of Baseline Cylinder | 39 |

| | Page |
|---|------|
| Figure 23 Velocity Profiles at 3/4 Diameter, Jet at 135 deg and Varying C_{mu} | 41 |
| Figure 24 Velocity Profile at 3/4 Diameters with Jet Exit at 70 with Varying C_{mu} | 42 |
| Figure 25 Velocity Profile at 3/4 Diameter with Jet Exit at 110 deg with Varying C_{mu} . | 43 |
| Figure 26 Jet at 90 deg with $C_{mu}=0.25$ | 43 |
| Figure 27 jet at 90 deg with $C_{mu}=1.02$ | 43 |
| Figure 28 Velocity Profiles with $C_{mu}=0.05$ and Varying Jet Location | 44 |
| Figure 29 Velocity Profiles with $C_{mu}=0.25$ and Varying Jet Location | 45 |
| Figure 30 Velocity Profiles with $C_{mu}=1.02$ and Varying Jet Location | 46 |
| Figure 31 Average Streamline Velocity for $C_{mu}=1.02$ at 70 deg, 90 deg, and 110 deg... | 46 |
| Figure 32 Velocity Profiles with $C_{mu}=3.11$ and Varying Jet Location | 47 |
| Figure 33 Average Streamline Velocity Plot of Case 1 | 48 |
| Figure 34 Average Streamline Velocity Plot of Case 2..... | 49 |
| Figure 35 Average Streamline Velocity Plot of Case 3..... | 49 |
| Figure 36 Average Velocity Profile at 1/2 Diameter of Cylinder..... | 51 |
| Figure 37 Average Velocity Profile with Standard Deviations at 1/2 Diameter | 52 |
| Figure 38 Average Velocity Profile at 3/4 Diameter..... | 52 |
| Figure 39 Average Velocity Profile with Standard Deviation at 3/4 Diameter..... | 53 |
| Figure 40 Average Velocity Profile at 1 Diameter | 53 |
| Figure 41 Average Velocity Profile with Standard Deviations at 1 Diameter | 54 |
| Figure 42 Ejection Phase of Jet | 55 |
| Figure 43 Vortex Mixing | 55 |
| Figure 44 Jet After Vortex Shedding..... | 56 |
| Figure 45 Suction Phase of Jet..... | 56 |

| | Page |
|--|------|
| Figure 46 Ejection Phase of Case 3 Synthetic Jet..... | 57 |
| Figure 47 Suction Phase of Case 3 Synthetic Jet..... | 58 |
| Figure 48 Far Field Average Streamline Velocity Plot of Baseline Cylinder | 59 |
| Figure 49 Case 1 Far Field Average Streamline Velocity Plot | 59 |
| Figure 50 Case 2 Far Field Average Streamline Velocity Plot | 60 |
| Figure 51 Case 3 Far Field Average Streamline Velocity Plot | 60 |
| Figure 52 Velocity Profile at 1 Diameter Aft of Cylinder..... | 61 |
| Figure 53 Average Velocity at .375 Hz | 65 |
| Figure 54 Average Velocity at 0.45 Hz | 65 |
| Figure 55 Average Velocity at 1 Hz | 65 |
| Figure 56 Average Velocity at 2 Hz | 65 |
| Figure 57 Average Velocity at 3 Hz | 66 |
| Figure 58 Average Velocity at 3.5 Hz | 66 |
| Figure 59 Stages Synthetic Jet Cycle for Case 2 | 68 |
| Figure 60 Velocity Profile at $\frac{3}{4}$ Diameter with Jet Exit at 0 deg and Varying C_{mu} | 74 |
| Figure 61 Velocity Profile at $\frac{3}{4}$ Diameter with Jet Exit at 45 deg and Varying C_{mu} | 74 |
| Figure 62 Velocity Profile at $\frac{3}{4}$ Diameter with Jet Exit at 90 deg and Varying C_{mu} | 75 |
| Figure 63 Velocity Profile at $\frac{3}{4}$ Diameter with Jet Exit at 180 deg and Varying C_{mu} | 75 |
| Figure 64 Velocity Profile at $\frac{3}{4}$ Diameter with $C_{mu}=0.04$ and Varying Jet Location..... | 76 |
| Figure 65 Velocity Profile at $\frac{3}{4}$ Diameter with $C_{mu}=1.59$ and Varying Jet Location..... | 76 |
| Figure 66 Velocity Profile at $\frac{3}{4}$ Diameter with $C_{mu}=2.29$ and Varying Jet Location..... | 77 |
| Figure 67 Velocity Profile at 3 Diameters Aft of Cylinder | 77 |
| Figure 68 Velocity Profile at 5 Diameters Aft of Cylinder | 78 |

List of Tables

| | Page |
|---|------|
| Table 1 Water Tunnel Specifications | 18 |
| Table 2 Synthetic Jet Parameters | 31 |
| Table 3 Tunnel Speed versus PIV Data | 34 |
| Table 4 Case Parameters | 48 |
| Table 5 Momentum Thickness of Cylinder Wake | 62 |

List of symbols

| <u>Symbol</u> | <u>Definition</u> |
|----------------------|--|
| A | Area (m^2) |
| C_D | Drag coefficient |
| C_L | Lift coefficient |
| C_P | Pressure coefficient |
| C_μ | Conventional Dimensionless Momentum Coefficient |
| $C_{\mu_{jms}}$ | Oscillatory momentum blowing coefficient |
| D | Diameter (m) |
| D_p | Drag force |
| dA | Differential in area (m^2) |
| dp | Differential change in pressure (Pa) |
| dt | Differential change in time |
| du_∞ | Differential change in free stream velocity |
| dx | Differential change in horizontal distance |
| F | Ratio of oscillation frequency to shedding frequency |
| F^+ | Dimensionless frequency |
| F^* | Non-dimensional excitation frequency |
| f | Oscillation frequency |
| f_s | Vortex shedding frequency |
| h | Width of jet orifice |
| i | x component |
| j | y component |
| P | Pressure (Pa) |
| R | Radius |
| Re | Reynolds Number |

| | |
|-----------------|--|
| Re_D | Reynolds number based on diameter |
| Re_{I_0} | Reynolds number based on impulse |
| St | Strouhal number |
| t | Time (sec) |
| U | Velocity (m/s) |
| U_∞ | Free stream Velocity (m/s) |
| u_0 | Stream wise velocity (m/s) |
| u_{jrms} | Root Mean Square of the jet velocity (m/s) |
| V | Velocity (m/s) |
| W | Weight (N) |
| x | Horizontal location |
| Δ | Change |
| ∂ | Partial derivative |
| γ | Ratio of specific heats |
| η | Efficiency |
| μ | Viscosity (kg/m s) |
| ν | Kinematics Viscosity (m^2 / s) |
| π | Turbine stage total pressure ratio |
| ρ | Density (kg/m ³) |
| τ | Time of discharge |
| ω | Angular velocity |
| θ | Angle |
| θ_{wake} | Wake Momentum Deficit |

Subscripts

| | |
|---|----------------------------|
| 0 | Total, stagnation, overall |
| D | Drag |
| L | Lift |

Abbreviations

| <u>Symbol</u> | <u>Definition</u> |
|----------------------|--|
| AIAA | American Institute of Aeronautics and Astronautics |
| DC | Direct Current |
| IA | Interrogation Area |
| ips | inches per second |
| MS-DOS | Microsoft Direct Operating System |
| PZT | Piezoelectric Transducer |
| NACA | National Advisory Committee for Aeronautics |
| PC | Personal computer |
| PIV | Particle Image Velocimetry |
| RMS | Root Mean Square |
| S-HGS | Silver coated Hollow Glass Spheres |
| USAF | United States Air Force |
| VR | Velocity Ratio |
| ZNMF | Zero-Net-Mass-Flux |

BOUNDARY LAYER CONTROL OF A CIRCULAR CYLINDER USING A SYNTHETIC JET

Chapter 1. Introduction

Flow control has long been a goal of engineers in many disciplines. Flow control on bluff bodies has been often studied because of its significant practical and theoretical interest. By controlling the boundary layer separation and the wake of bluff bodies there is the great potential to modify the aerodynamic shape and characteristics thus improving their efficiency (1). An important attribute of active control of the apparent shape of aerodynamic surfaces is that it could potentially lead to unconventional aerodynamic design approaches that are driven primarily by mission constraints such as stealth payload and volume. The reduced aerodynamic performance of such unconventional shapes that may stall at small angles of attack can be augmented by the use of flow control to maintain aerodynamic performance throughout their flight envelope (7).

One of the most studied bluff bodies is a circular cylinder. The flow structure around a circular cylinder is a classical and important problem in engineering. It is often associated with vortex shedding and flow instability causing unsteady forces on the cylinder. Numerous experimental and theoretical studies have provided vast amounts of data on fluid flow around circular cylinders. The aim of this research effort is to use a synthetic jet to control the boundary layer of a circular cylinder at a moderate Reynolds number of 5800.

1.1 Background

Synthetic jets also known as zero-net-mass-flux oscillatory momentum generators or zero-net-mass-flux jets have been used as a versatile tool for active flow control for the past decade with applications as diverse as separation control, thrust vectoring, mixing, and heat transfer. These devices are typically used to generate large coherent structures in shear flows, promoting transition, introducing unsteady harmonic or pulsating motion into a turbulent shear flow, or even generating turbulent jets through entrainment of still fluid (11).

The driving mechanism for synthetic jets typically falls into three categories: PZT, oscillating piston, and a hybrid design. The first is the use of a piezoelectric driver to oscillate a small diaphragm in a shallow cavity at frequencies on the order of 1000 Hz. The piezoelectric ceramic material, PZT, responds to the input voltage signal by contracting or expanding, causing the membrane to oscillate (11). Synthetic jet actuators based on PZT technology have been used extensively by researchers at Georgia Institute of Technology. Amitay et al. used a pair of fluidic actuators based on synthetic jet technology that emanated radially from a two-dimensional cylinder to modify the aerodynamic shape of the cylinder in a wind tunnel. They demonstrated that at low Reynolds numbers ($Re_D = 4000$) that the closed recirculation flow regimes near the surface scale with the momentum coefficient and can displace local streamlines well outside the surface boundary layers. Based on azimuthal surface pressure distributions measured at higher Reynolds numbers ($Re_D = 75,500, C_\mu = 6 \times 10^{-4}$) over a range of jet angles, they showed the jets effect substantial concomitant increase in lift (up to

$C_L = 0.55$) and a reduction in drag of up to 30% when the jets were located between the front stagnation point and the zone of separation(1). Further studies showed these jets were also effective at $Re_D = 131,100$. Additional studies by Atimay et al. found that “depending on the formation frequency, its interaction with the cross flow can lead to the formation of a closed recirculation region, or an open stream wise domain that is characterized by a train of several successive vortices which are advected along the surface of the cylinder until the vortices weaken and disappear” (2). As a result of the cross flow being accelerated around the interaction domain, the downstream surface boundary layer becomes thinner, allowing the flow to overcome stronger adverse pressure gradients, resulting in delayed flow separation. The separation point of the flow over the cylinder moved from approximately 91° to 111° relative to the free stream (7).

Hononnan et al. performed additional experiments using an airfoil attached to the synthetic jet cylinder in a wind tunnel at a chord Reynolds number of 310,000 that showed that the lift to drag ratio had two distinct regions depending on the actuation frequency. The actuation frequency in the first regime is of the same order as the shedding frequency of the airfoil, and L/D_p decreases with increasing forcing frequency. In the second regime, the actuation frequency was at least an order of magnitude higher than the shedding frequency, and the L/D_p was nominally 35% higher than at the lower actuation frequencies and was invariant with the forcing frequency (7).

The second class of synthetic jet actuators are those driven by an oscillating piston in a cylinder to create pressure oscillations resulting in the formation of a synthetic jet. Tomar et al. successfully used an oscillating piston in a cylinder to create a synthetic jet in crossflow (15). The piston was connected via a coupling to a scotch-yoke

mechanism that was driven by a computer controlled stepper motor. This jet had a frequency range of 0.5 to 6 Hz. A similar setup was used by Tuck et al. to create a synthetic jet in the leading edge of a NACA 0015 to increase the stall angle of the airfoil from 10° to 18° , which resulted in a maximum lift coefficient increase of 46% above the uncontrolled lift coefficient (16).

Rao et al. devised a novel approach that combined the best features of PZT based synthetic jets and the piston cylinder based synthetic jets. This design used a DC motor with its shaft connected eccentrically to a piston which was connected to the membrane of the synthetic jet actuator. The design offered significant benefits over PZT based synthetic jets. This setup achieved larger membrane oscillation amplitudes of at least an order of magnitude higher than the PZT actuators. It eliminated the dependence of oscillation amplitude on the oscillation frequency, which plagues PZT mechanisms. Through the use of state-of-the-art, high density electric motors it competed with the power densities of PZTs, while it required significantly lower driving voltages (11).

1.2 Objective

The goal of this research effort was to determine the effects of a synthetic jet on the flow around a circular cylinder. The synthetic jet created a pair of counter rotating vortices that interacted with the boundary layer of the circular cylinder. The main objective of this research was to find a location on the cylinder where a combination of jet exit velocity and frequency delays the separation of the boundary layer. In order to achieve this goal a synthetic jet was designed and manufactured. In addition, setup and verification of the experimental water tunnel and PIV data collection hardware and software was completed.

1.3 Organization

This research effort will present and explain the theory behind a cylinder in cross flow and synthetic jets in Chapter 2. The following chapters discuss the experimental setup, including the facilities, hardware, software, and measurement devices used during the course of the research. The design of the synthetic jet actuator is also discussed. The setup and operation of the water tunnel and the particle image velocimetry (PIV) equipment is explained. The impact of the jet orifice placement, exit velocity, and frequency of the jet are discussed. Results from the data collection process are examined and conclusions presented on the effectiveness of the synthetic jet used in this research. Recommendations for future research are presented.

Chapter 2. Theory

The relevant theory behind the different aspects of this research is briefly discussed. The information discussed in this chapter is by no means all inclusive. Refer to the cited works for more in-depth descriptions of presented topics.

2.1 Cylinder Boundary Layer and Wake

A circular cylinder in cross flow is a common and often studied fluid flow problem. The free stream fluid is brought to a rest at the forward stagnation point at 0° , with an accompanying rise in pressure. From the stagnation point, the pressure decreases with increasing surface distance, x , and the boundary layer develops under the influence of a favorable pressure gradient ($dp/dx < 0$). However, the pressure must eventually reach a minimum, and toward the rear of the cylinder further boundary layer development occurs in the presence of an adverse pressure gradient ($dp/dx > 0$). From $U_\infty = 0$ at the stagnation point, the fluid accelerates because of the favorable pressure gradient ($dU_\infty/dx > 0$ when $dp/dx < 0$), reaches a maximum velocity when $dp/dx = 0$, and decelerates because of the adverse pressure gradient ($dU_\infty/dx < 0$ when $dp/dx > 0$). As the fluid decelerates, the velocity gradient at the surface eventually becomes zero. This location is called the separation point, and the fluid near the surface lacks sufficient momentum to overcome the pressure gradient and continued downstream movement is impossible. Since the oncoming fluid also precludes flow back upstream, boundary layer separations must occur. At this condition, the boundary layer detaches from the surface

of the cylinder, and a wake is formed in the downstream region. Flow in this region is characterized by vortex formation and is very irregular. The separation point is the location for which $(\partial u / \partial y)_s = 0$ (8). Figure 1 and Figure 2 show boundary layer separation over a circular cylinder.

The occurrence of boundary layer transition, which depends on Reynolds number, strongly influences the position of the separation point. For the circular cylinder the characteristic length is the diameter, and the Reynolds number is defined as

$$\text{Re}_D \equiv \frac{\rho U_\infty D}{\mu} = \frac{U_\infty D}{\nu}. \quad (1)$$

Since the momentum of the fluid in a turbulent boundary layer is larger than in the laminar boundary layer, it is reasonable to expect transition to delay the occurrence of separation. If $\text{Re}_D < 2 \times 10^5$, the boundary layer remains laminar, and separation occurs at $\theta \approx 80^\circ$. However, if $\text{Re}_D > 2 \times 10^5$ then boundary layer transition occurs, and separation is delayed to $\theta \approx 140^\circ$ (8).

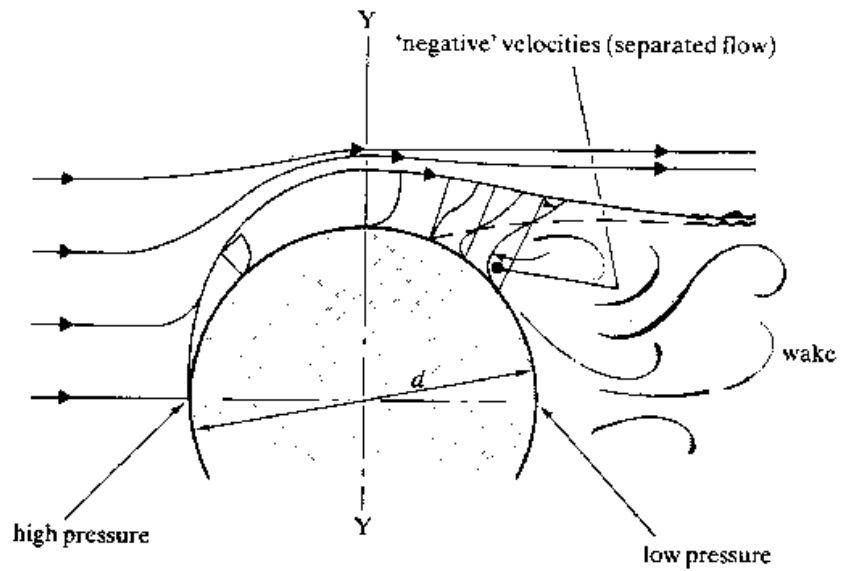


Figure 1 Boundary Layer Separation on a Cylinder (4)

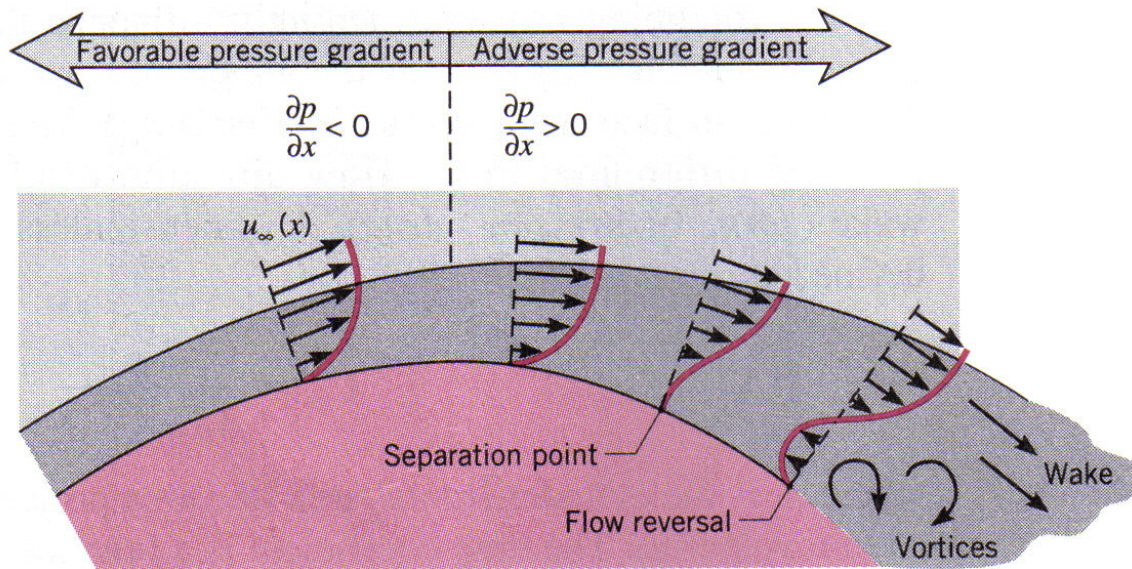


Figure 2 Close-up View Boundary Layer Separation on a Cylinder (8)

Near the widest section of the cylinder, the boundary layers separate from each side of cylinder surface and form two layers that trail aft in the flow and bound the wake.

Since the innermost portion of the shear layers, which is in contact with the free flow, the shear layers roll into the near wake, where they fold on each other and coalesce into discrete swirling vortices. Immediately behind the cylinder, a recirculation region exists with a strong reversing flow. The region between the cylinder and the end of the recirculation region is called the vortex formation region. The centerline velocity becomes zero at the end of the vortex formation region. The two separated shear layers merge downstream of the cylinder and the velocity profile presents a typical wake profile. Figure 3 depicts the progression of the wake aft of a cylinder. A regular pattern of vortices, called a vortex street, trails aft in the wake.

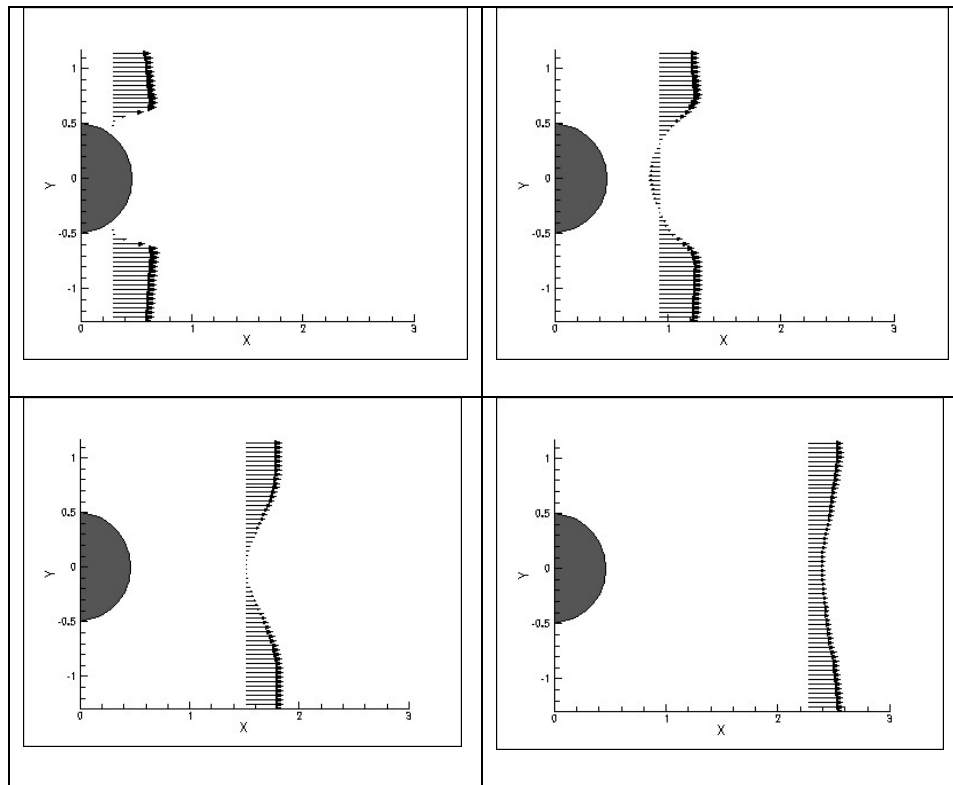


Figure 3 Progression of the Wake Behind a Cylinder (12)

The wake aft of a circular cylinder in a steady subsonic flow is a function of Reynolds number. The Reynolds number of the flow examined in this research is within

the Reynolds number range $300 < Re < 1.5 \times 10^5$, and is termed sub critical. In this range, the vortex shedding is strong and periodic, but the wake is turbulent.

The frequency of the vortex shedding can be determined using the Strouhal number. The Strouhal number is the dimensionless proportionality constant between the predominant frequency of vortex shedding and the free stream velocity divided by the cylinder width (18),

$$St = \frac{f_s D}{U_\infty}. \quad (2)$$

The Strouhal number of a stationary cylinder in a subsonic flow is a function of Reynolds number and surface roughness and free stream turbulence. This relationship is shown in Figure 4. The Strouhal number for the test condition Reynolds number of 5800, which is based on a cylinder diameter of 0.051 m and a free stream velocity of 0.114 m/s, is 0.2. The vortex shedding frequency, f_s , for the test case is 0.45 Hz.

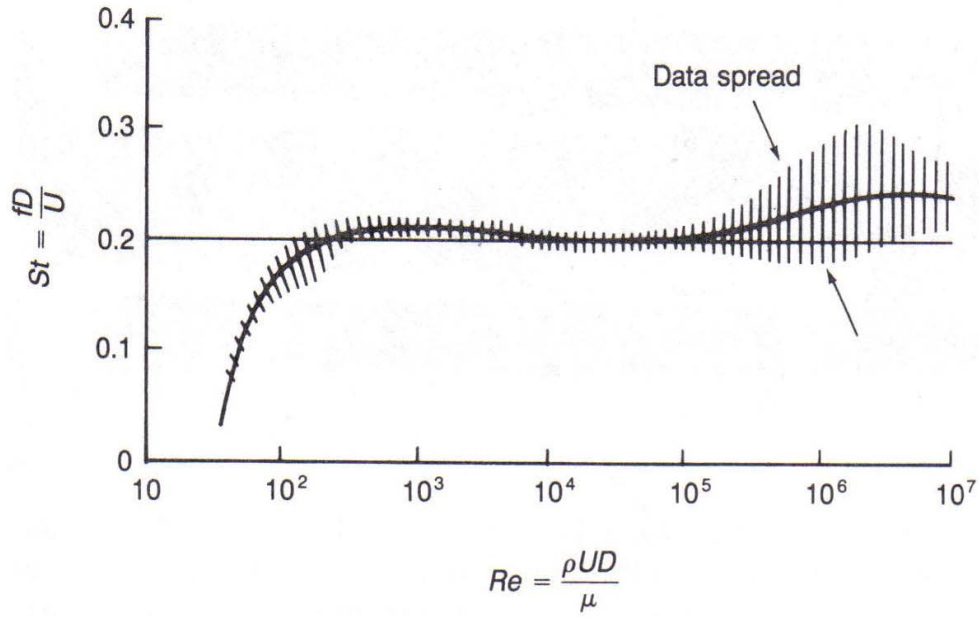


Figure 4 Strouhal Number versus Reynolds Number for Flow Around a Cylinder (18)

2.2 Synthetic Jet Theory

Synthetic jets are also known as zero net mass flux (ZNMF) jets. Unlike conventional continuous jets or pulsed jets, a unique feature of synthetic jets is that they are formed from the working fluid of the flow system in which they are developed, and thus transfer linear momentum to the flow system without net mass injection across the system boundary (14). A synthetic jet is formed by the interactions of a train of vortices that are formed by alternating momentary ejection and suction of fluid across an orifice such that the net mass flux is zero. The flow during the suction stroke is similar to the flow induced by a sink that is coincident with the jet orifice, while the flow during the ejection stroke is primarily confined to a finite narrow domain in the vicinity of the jet center line. During the ejection stage, the flow separates at the sharp edges of the orifice and forms a vortex sheet that rolls into a pair of counter rotating vortices that move away from the orifice under its self-induced velocity. The interaction between the vortex and the

reversed flow caused by the suction of fluid when the pressure drop across the orifice is reversed depends on the strength of the vortex and the distance from the orifice (1).

The counter rotating vortices can be characterized by two primary dimensionless parameters. The first is the dimensionless “stroke” length, L_0 / d (14)

$$L_0 = \int_0^{\tau} u_0(t) dt. \quad (3)$$

where $u_0(t)$ is the stream wise velocity, τ is the time of discharge, and d is the characteristic length scale of the orifice. The second parameter is the Reynolds number based on impulse which is the momentum associated with the discharge and is given by (14)

$$\text{Re}_{I_0} = I_0 / \mu d \quad (4)$$

where I_0 is given by (14)

$$I_0 = \rho \int_0^{\tau} \int_A u_0^2(\bar{x}, t) dA dt. \quad (5)$$

When the vortices are formed time-periodically to synthesize a jet, an important formation parameter is the repetition rate or the formation frequency, f , where the dimensionless frequency is given by (14)

$$F^* = f I_0 / (\rho v^2). \quad (6)$$

F^* is a measure of the total impulse per unit time and may be used as a parameter that characterizes different jets according to their strength.

2.2.1 Synthetic Jet in Cross Flow

A synthetic jet is able to cause changes in the flow through the addition of momentum to the boundary layer. The synthetic jet adds momentum to the boundary layer in two ways. During the suction phase of the cycle, the jet draws the low momentum fluid in the boundary layer inside the cavity, bringing the higher momentum fluid at the boundary layer edge closer to the surface. During the blowing phase of the cycle, the jet adds the same fluid with higher momentum to the flow. The average momentum added over the cycle replenishes the momentum deficit in the boundary layer (11). In addition to the jet producing momentum, it also enhances the ability of the boundary layer to overcome adverse pressure gradients downstream through the induced mixing of the low momentum fluid near the surface with the high momentum external flow (2).

A synthetic jet in a cross flow can be characterized by the following non-dimensional groups. The first is the non-dimensional excitation frequency, which is defined as (15)

$$F^+ = \frac{fD}{U_\infty}. \quad (7)$$

The oscillatory momentum blowing coefficient is another significant parameter because it is a measure of the momentum imparted on the flow by the synthetic jet normalized by a characteristic momentum for the unexcited flow (15)

$$c_{\mu_{jrms}} = 2 \frac{h}{D} \left(\frac{u_{jrms}}{U_\infty} \right)^2. \quad (8)$$

An alternative measure of the strength of the synthetic jet is the velocity ratio defined as
(15)

$$VR = \frac{u_{jrms}}{U_{\infty}}. \quad (9)$$

Another important measure of synthetic jet performance on the flow over a circular cylinder is the ratio of oscillation frequency to the natural shedding frequency denoted by f_s .

$$F = \frac{f}{f_s}. \quad (10)$$

2.3 Particle Image Velocimetry

Particle Image Velocimetry (PIV) is a whole-field measurement technique providing instantaneous velocity vector measurements in a cross section of a flow. A PIV setup consists of three main components: a laser, a camera, and flow visualization software. A laser is pulsed through a cylindrical lens to produce a laser light sheet. The laser light sheet is positioned along the plane of interest in the flow. The laser must be powerful enough to illuminate the particles so that the particles can be detected by the camera. The camera used must be focused on the same plane as the laser light in order to capture valid images. The flow visualization software controls the timing of the laser, the camera and then processes the flow field images. PIV imaging software is based on the equation (5):

$$V = \frac{\Delta x}{\Delta t}. \quad (11)$$

The software measures the distance traveled by particles in the flow within a known time interval. The particle seeded flow is illuminated in the target area by a laser light sheet. The light sheet is pulsed to produce a stroboscopic effect, freezing the movement of the seeding particles. The time between the laser pulses is the denominator in eqn (11). A Charged Coupled Device (CCD) camera is positioned at right angles to the flow in order to detect the position of the illuminated particles. The pulsing light-sheet and camera are synchronized so that particle positions at the instant of light pulse number 1 are registered on frame number 1, and particle positions from pulse number 2 are on frame 2.

Once a sequence of light images is recorded, the images are divided into subsections called interrogation areas (IA). The interrogation areas from each frame are correlated to produce an average particle displacement vector. This process is accomplished for all of the interrogation errors to produce a vector map of the average particle displacement. The displacement vectors are converted to velocity vectors by dividing by the known time interval between image captures. The 2-D setup used for this research produces horizontal (x) and vertical (y) velocities. The third velocity component, which was not measured during this research project, can be obtained by using a second camera to achieve a 3-D velocity vector map. A variety of techniques can be used to produce vector maps based on the recorded images.

Adaptive correlation was used to produce the velocity vector maps for this research. Adaptive correlation is an advanced image processing technique that has a number of benefits over using standard PIV correlation techniques. Adaptive correlation captures the particle images that left the interrogation area during the time between the

two light pulses. The loss of these particle images is known as in-plane dropout, which reduces signal strength and the number of successful vectors that can be obtained. Capturing more particle images for each vector permits the interrogation area to be refined while still obtaining an adequate number of successful vectors without increasing the seeding density in the flow. The downside of using adaptive correlation is the longer processing time when compared to less sophisticated techniques. In addition, noise has a greater impact when using adaptive correlation. (5)

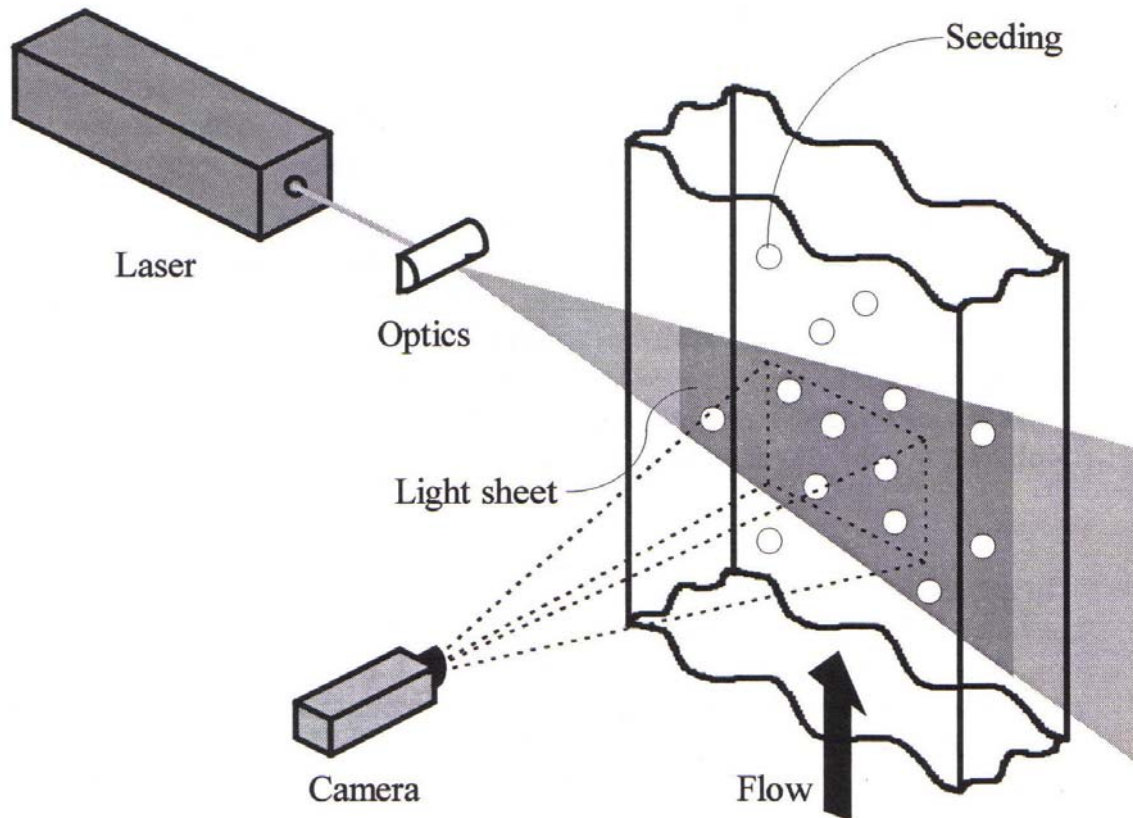


Figure 5 Typical PIV Setup (5)

2.4 Scotch-Yoke Theory

The synthetic jet used in this research was formed by the motion of a piston in a cylinder that was driven by stepper motor via a Scotch-Yoke mechanism. The Scotch-Yoke is a device which can produce pure sinusoidal back and forth motion from a constant rotational motion. The velocity of the peg sitting on the periphery of a rotating wheel of radius R and constant angular velocity ω is

$$V=R[j\cos(\omega t)+i\sin(\omega t)] \quad (12)$$

The slot in which the peg slides is part of larger rigid body confined to move strictly in the x direction by the shown constraints. The axial position the slot takes is then simply the x component of V integrated over time.

$$x=R\sin(\omega t) \quad (13)$$

The result is pure sinusoidal motion and velocity profile (12).

Chapter 3. Experimental Setup and Procedure

Several pieces of equipment were used in the course of the research. The most important are discussed in this section. After the descriptions of the equipment used, the experimental procedure used for data collection is described.

3.1 Water Tunnel

The water tunnel used for the research is a Rolling Hills Research Corporation Model 0710 University Desktop Water Tunnel serial number 0020. The water tunnel is located on the AFIT campus in building 644 in room L154, Wright–Patterson Air Force Base, Ohio. The tunnel offers views of the test section through one downstream window and two side windows, all made of tempered glass. The tunnel features a variable speed motor, a turbulence reducing screen and honeycomb in the settling chamber, a 6:1 contraction ratio, and dual line return plumbing. Table 1 lists the specifications of the water tunnel. A photograph of the water tunnel and various components used for this research is shown in Figure 6.

Table 1 Water Tunnel Specifications

| Tunnel Specifications | |
|------------------------------|---|
| Length | 112 inches |
| Width | 46 inches |
| Height | 47 inches |
| Weight | Approximately 900 lb _f w/water |
| Capacity | 105 gallons |
| Test Section | 7 inches x 10 inches x 18 inches |
| Down Stream Window | 7 inches x 9.5 inches |
| Flow Velocity | 0 to 5 inches per second |
| Centrifugal pump | 1.5 horsepower, 115 volts, 16 amps |
| Dye System | Pressurized 3 color |
| Table | Steel with lockable swivel casters |



Figure 6 Water Tunnel and Experimental Setup

The water tunnel came pre-calibrated to ensure that the digital speed control shows the speed of the water in the test section. The graph below is the calibration chart for the AFIT water tunnel. The graph shows the tunnel speed in inches per second versus the frequency of the motor. The velocity of the flow in the test section used in this study was 4.5 inches per second.

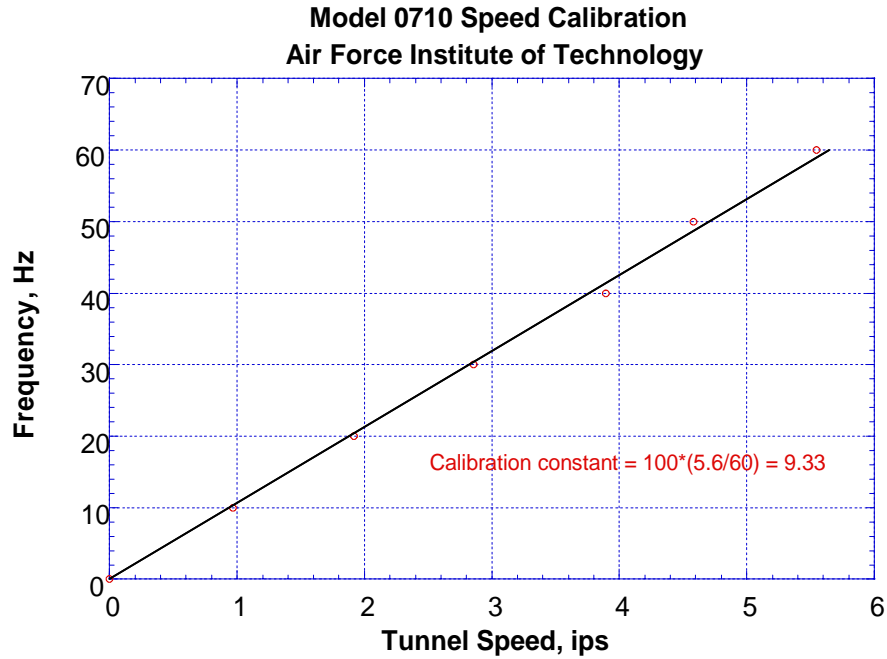


Figure 7 Motor Frequencies versus Water Tunnel Speed (17)

3.2 Synthetic Jet Components

3.2.1 Cylinders

Two clear acrylic cylinders were used in the course of this research. The cylinders are shown in Figure 8. Both cylinders had a diameter of 5.08 cm and a length of 16.51 cm, which results in an aspect ratio of 3.25. The cylinder length allowed the cylinders with the wall mounts to span the entire test section. This configuration ensured that the flow field around the cylinder was ideally free from 3-dimensional effects which are caused by the generation of tip vortices. A baseline cylinder was used to determine the flow characteristics around an un-modified cylinder and then compared to the results of the cylinder that had been modified with the synthetic jet. The baseline and synthetic jet cylinder can be seen in Figure 8. The exit slot for the synthetic jet has a width of 1.6

mm, a length of 82.55 mm, and was oriented normal to the surface of the cylinder. The exit slot can be seen in Figure 9. The relative slot width used in this investigation was $h/D = 3.125\%$. The slot width was minimized in order to maximize jet velocity for the same displacement of fluid, because it was believed that the control would be more effective at higher exit velocities and would minimize the effect of the slot on the boundary layer. The slot does not span the entire length of the cylinder. The slot was located 50 mm from the edge of the cylinder with the pipe fitting and 31.75 mm the other edge of the cylinder. A 12.7 mm diameter chamber was machined into the acrylic cylinder. The chamber was parallel to the longitudinal axis of the cylinder and the jet exit slot and has a length of 125 mm. The hollow chamber was connected to another 12.7 mm chamber that is located 19.05 mm from the end of cylinder and was perpendicular to the exit slot. Attached to the end of the hollow chamber was a plastic pipe fitting that was connected to 12.7 mm diameter Tygon tubing. The two chambers and the tubing connected the exit slot to the driving mechanism which supplied the pressure oscillations to create the synthetic jet. The pipe fitting was painted flat black in order to reduce reflection from the laser.



Figure 8 Baseline Cylinder (Left) Synthetic Jet Cylinder (Right)

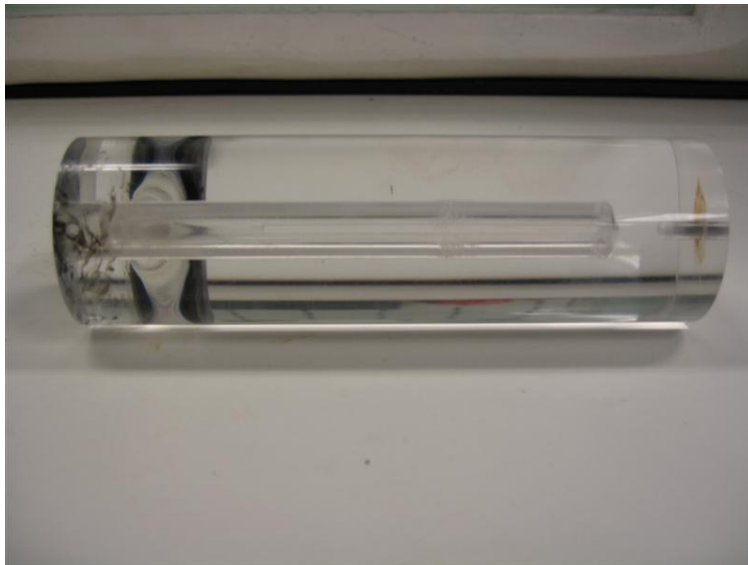


Figure 9 Synthetic Jet Cylinder

The cylinders were secured in place by wall supports that were manufactured by Rolling Hills Research. The cylinders were attached to the supports by sliding the pivot pins into the ball bearings at the bottom of the wall plates. The ball bearings allowed the cylinder to be rotated to place the synthetic jet exit at various angles relative to the flow.

The supports were made of clear plastic that resulted in minimal interference during data collection. The wall supports were mounted on the water tunnel to place the cylinders 11 cm aft of the start of the test section. Figure 10 shows the synthetic jet cylinder mounted in the water tunnel.

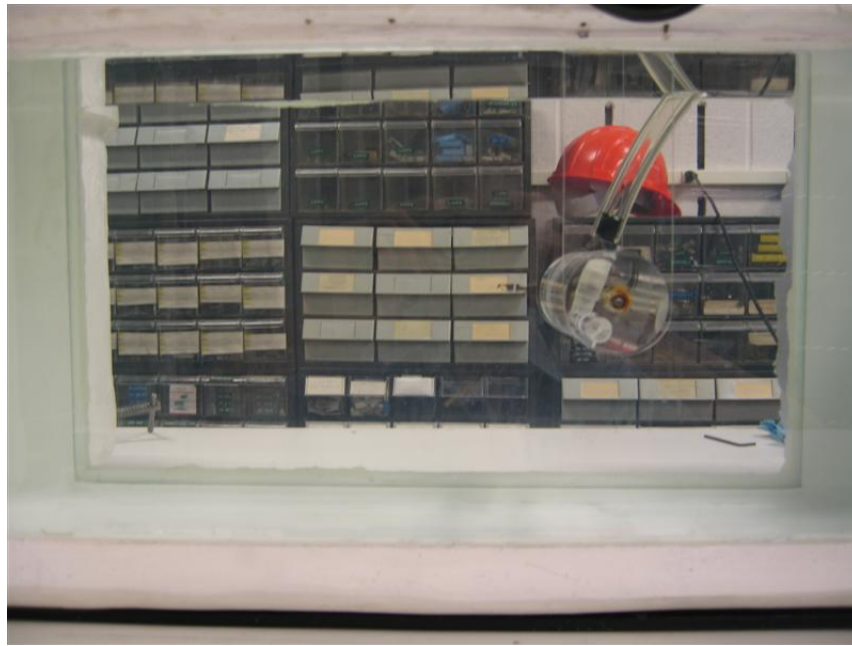


Figure 10 Synthetic Jet Cylinder Mounted in the Test Section

3.2.2 Piston, Cylinder, and Scotch-Yoke Mechanism

The pressure oscillations were supplied by a 25.4 mm diameter piston/cylinder arrangement that was driven by a computer controlled stepper motor via a Scotch-Yoke mechanism. The entire system is shown in Figure 11. The cylinder had a length of 100 mm, and the piston had a shaft length of 80 mm. The piston was fitted with two rubber O-rings to ensure a tight seal in the cylinder. The Scotch-Yoke mechanism used in the research was comprised of an aluminum mounting disk that attached to the stepper motor by sliding the disk over the motor shaft and was secured to the motor shaft by a set screw. A 6.35 mm steel peg extended from the mounting disk. The peg was located 13.5 mm

from the center of the mounting disk. The distance resulted in a 27 mm stroke length. The Scotch-Yoke mechanism translated the rotational motion of the stepper motor shaft into linear motion of the piston with a sinusoidal velocity profile as described in Sec 2.4. The entire assembly was secured to a metal mounting board that was placed on top of the water tunnel.

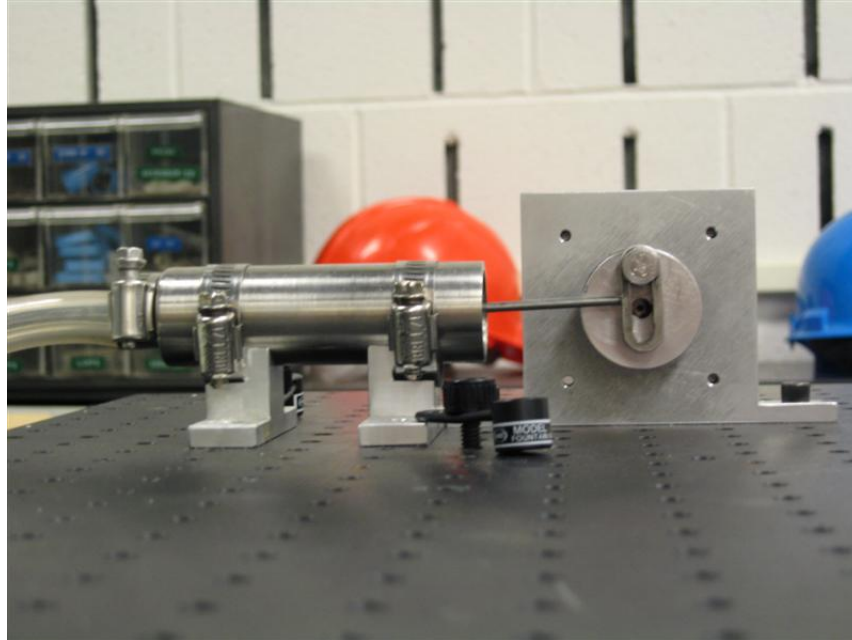


Figure 11 Scotch-Yoke Mechanism, Piston, and Cylinder

3.2.3 Stepper Motor

An Arrick Robotics stepper motor system was used to drive the synthetic jet used in the research. A stepper motor was used because it allows for precise positioning and speed control under digital computer control. The motor had four copper coils which created a magnetic field when energized. The field reacted to the permanent magnet connected to the shaft of the motor and caused the motor shaft to rotate. The sequence in which the coils were energized determined the step angle and direction. The motor

advanced one step as each new phase pattern was sent. An additional benefit of using a stepper motor is that they are constructed to be maintenance free and have a long motor life. Stepper motors cannot be harmed or overheated by stalling or binding of the shaft.

(9)

The Arrick Robotics model MD-2b motor was used. The motor case had a 57.15 mm diameter and was 101.6 mm inches long. The motor shaft was 6.35 mm in diameter and 19.05 mm in length. The motor was operated in half step mode resulting in a step size of 0.9 degrees. One full revolution of the shaft was 400 steps. The speed maximum motor speed used during the experiments was 1400 steps per second or 3.5 revolutions per second, and the minimum motor speed used was 150 steps per second or 0.375 revolutions per second. The stepper motor was secured to metal plate by a mounting bracket.

The stepper motor was controlled by the MD-2 driver box and an Intel Centrino laptop. The laptop computer connected to the driver box via the laptop computer parallel printer port. The driver box was then connected to the stepper motor. The speed and position of the stepper motor was set by a MS-DOS based program, also provided by Arrick Robotics. The program allowed the user to set the motor speeds in steps per second and position in terms of steps.



Figure 12 Stepper Motor

3.3 Particle Image Velocimetry

3.3.1 Laser and Light Arm

The laser used for PIV was a New Wave Research Solo 120 Nd:YAG with two heads in one unit. Each laser has a peak energy level of 120 mJ at a wavelength of 532 nm while operating at 15 Hz. The laser was set to high power for all data runs to ensure there was sufficient light energy for the camera to capture useful images of the fluid flow. The laser light was directed to the test section of the water tunnel by a Dantec Dynamics, Inc. high power light guiding arm. At the end of the light arm was a Dantec Dynamics modular light sheet optics which shaped and focused the laser beam. The optics transformed the laser beam into a laser light sheet and had an adjustment knob to adjust the width of the laser light sheet. The optics were positioned to aim the light sheet through the window at the end of the tunnel to produce a vertical light sheet that covered the entire test section of the tunnel along the test section's centerline.



Figure 13 Laser and Light Arm

3.3.2 Seeding Particles

The seeding particles used in the flow are Dantec Dynamics Silver coated Hollow Glass Spheres (S-HGS). The spheres are borosilicate glass particles with a spherical shape, a smooth surface and a thin silver coating to increase reflectivity. The size distribution of the particles ranges from 2-20 μm , with a mean diameter of 10 μm , and a density of 1.4 g/cm^3 . The density of the particles is greater than the density of the water used in the tunnel, which resulted in the particles settling to the bottom of the tunnel over a period of time. Prior to using the PIV system, the particles had to be agitated to ensure that a sufficient number were evenly distributed in the flow.

3.3.3 Video Capture

A Redlake MegaPlus ES 4.0/E 12 bit CCD camera was used to capture the images of the seed particles that were illuminated by the laser light sheet. Dantec Dynamics System Hub controlled the timing of the camera and the laser. The camera has a

resolution of 2048 x 2048 pixels and a pixel size of 7.4 μm . The camera was attached to a tripod that allowed the camera setup to be easily placed for the different flow field views. Images were taken at two different camera positions. The first position was used to examine the boundary layer around the cylinders. The second camera position was used to capture the wake of the cylinder in entire test section. A 105 mm Nikon lens was used for the near field flow visualization and a 60 mm Nikon lens was used for far field flow visualization.

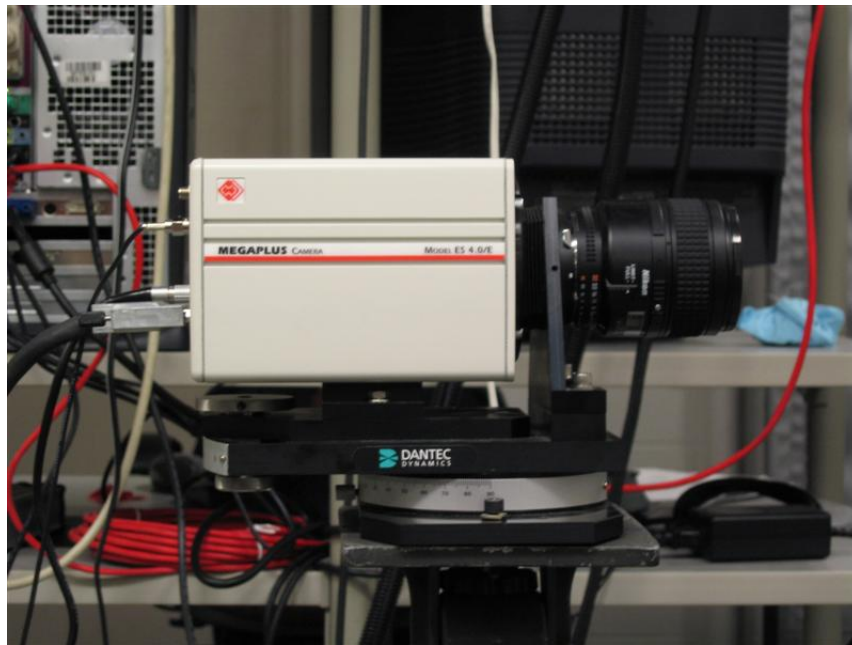


Figure 14 Redlake Camera

3.3.4 Image Processing

The image pairs were imported to a Pentium computer by the Flow Manager System Hub. The system hub controls the synchronization and image acquisition. The unit also provides the communication links between the hub, the laser, camera and

application computer. A 100 Mbit Ethernet adapter was used to transfer the images from the hub to the application computer.

The image pairs were processed by Dantec Dynamics Flow Manager software, after they were downloaded from the Hub. The field of view was set to 64.3 mm for the first camera position and 302.5 mm for the second position. The field of view must be correctly set in order ensure correct values of flow velocity and vorticity. The acquisition control was set to 1000 μs between laser pulses, 2 laser pulses per recording, 0.01 μs laser pulse, and 133.3 ms between recordings for the camera position 1. The only acquisition control parameter that changed for the second camera position was the time between pulses; the time was increased to 3000 μs

The Flowmap software was used for data processing after the image pairs were collected. Image masking was used when the cylinders were in the flow. This procedure removed data that were of no interest. The masking technique was used to remove the vectors produced by reflections off of the cylinders. The adaptive correlation technique then was used to produce vector maps of the flow. Additional post processing procedures could be applied to the vector maps

3.4 Experimental Procedure

3.4.1 Data Collection Procedure

PIV was the sole means of data collection for the research. The camera had to be focused on the same plane as the laser light sheet prior to collecting data. In addition, the field of view had to be measured at each camera location. Once the camera was setup, the water tunnel was turned on, and allowed a 5-minute warm-up period to ensure steady flow and to allow the seeding particles to be evenly distributed in the flow. Various

water tunnel speeds were set to determine if the speed set with the tunnel speed controller matched the velocities measured by the PIV system. The synthetic jet cylinder was then placed in the tunnel's test section. The synthetic jet was activated prior to data collection. The jet was activated by operating the stepper motor at a programmed speed and stroke length distance. After the jet was activated, PIV recording was initiated. The PIV system stopped acquiring images after 75 image pairs were captured. Another stepper motor program was then used to achieve a different exit velocity and frequency. The process was then repeated until all the test points per jet exit position were completed. The jet exit slot position was changed, and additional PIV data were collected at the same jet parameters.

The position of the camera was changed to gather additional data at the same jet exit locations, jet velocities, and frequencies. The camera was refocused and the field of view was changed every time the camera was repositioned. The second camera location captured the entire test section aft of the cylinder to determine what effects the jet had on the wake of the cylinder.

Quiescent flow data were also collected at each camera location to determine the effects of the synthetic jet on the surrounding fluid without the presence of cross flow.

3.4.2 Test points

Data collection for the synthetic jet in cross stream was taken with the jet exit at seven different angular locations, eight different input frequencies and two camera locations. The exit slot was placed at 0° , 45° , 70° , 90° , 110° , 135° , and 180° relative to the free stream. The locations of the jet exit slot are shown in Figure 15. Table 2 contains the parameters of the synthetic jet in the cross flow. The values in Table 2 were

calculated using a Matlab program based on equations 12 and 13. The Matlab code is provided in Appendix B. In addition, synthetic jet data was collected in quiescent conditions with the jet oriented 180 degrees from the free stream flow. The stroke length of the piston was constant at 2.7 cm. The pressure oscillation frequency was varied from 0.375, 0.45, 1, 2, 2.5, 3, and 3.5 Hz. The unmodified acrylic cylinder was also used in the cross flow at each camera location as a performance baseline for the synthetic jets performance.

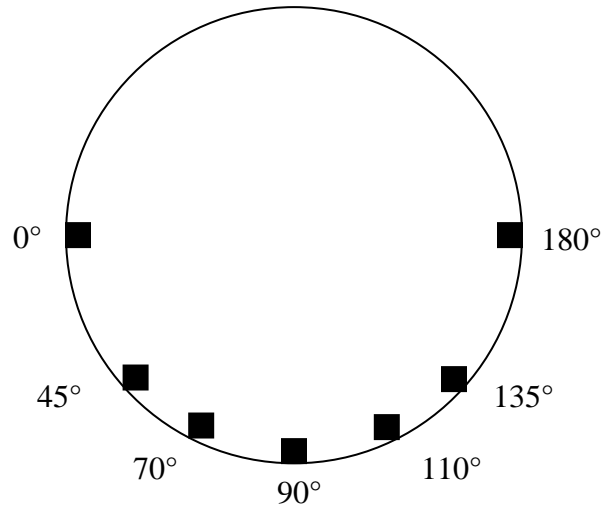


Figure 15 Location of Angular Positions of Synthetic Jet

Table 2 Synthetic Jet Parameters

| Oscillation Frequency (Hz) | 0.375 | 0.45 | 1 | 2 | 2.5 | 3 | 3.5 |
|----------------------------|-------|------|------|------|------|------|------|
| max jet velocity (m/s) | 0.12 | 0.15 | 0.33 | 0.65 | 0.81 | 0.98 | 1.14 |
| jet rms velocity (m/s) | 0.09 | 0.10 | 0.23 | 0.46 | 0.58 | 0.69 | 0.81 |
| C _{mu} | 0.04 | 0.05 | 0.25 | 1.02 | 1.59 | 2.29 | 3.11 |
| VR | 0.76 | 0.91 | 2.02 | 4.04 | 5.05 | 6.06 | 7.07 |
| F _{plus} | 0.17 | 0.2 | 0.45 | 0.90 | 1.12 | 1.34 | 1.57 |
| F | 0.84 | 1 | 2.24 | 4.47 | 5.59 | 6.71 | 7.83 |

Chapter 4. Results

The following sections compare the effects of the synthetic jet on the boundary layer and the wake of the circular cylinder. The comparisons were made at seven slot positions and seven different oscillation speeds and frequencies which are shown in Table 2. Two camera positions were used to collect PIV data. After the 98 test conditions were performed the data were analyzed. The PIV data used to generate whole field images. In addition, the PIV data was also used to generate velocity profiles at six locations in the flow. The velocity profiles were examined at the $\frac{1}{2}$, $\frac{3}{4}$, and 1 diameter locations on the cylinder and 1, 5 and 5 diameters aft of the cylinder. Based on the vector plots and the velocity profiles the 98 test conditions trends were noticed about how the jet affected the boundary layer based on frequency and jet location. Three cases were chosen for further study. All three cases helped the flow to overcome the adverse pressure gradient that caused flow separation and caused a decrease in the momentum deficit. Case 1 is with the jet exit slot at 70° with a $C_{\mu jrms} = 1.03$. Case 2 has the slot at 110° with a $C_{\mu jrms} = 0.25$. Case 3 has the jet exit slot is located at 135° on the cylinder and a $C_{\mu jrms} = 3.11$. The results discussed are the mean of seventy five images pairs.

4.1 Determining the Free Stream Flow Velocity

Prior to performing any tests with the circular cylinder in the water tunnel, the PIV system was used to determine the free stream velocity of the water at different velocity settings. The tunnel speed setting is displayed in inches per second, and the PIV

system displays velocity in meters per second. In order to maintain consistent units all data will be presented using SI units. During calibration the flow velocity was set to speeds of 0.14, 0.13, 0.10, 0.076, 0.051, 0.025, 0.013, and 0 m/s (5.5, 5, 4, 3, 2, 1 and 0 inches per second respectively). 100 images were collected at each speed setting, and the data was averaged to determine the velocity of the flow. The results are shown in Figure 16.

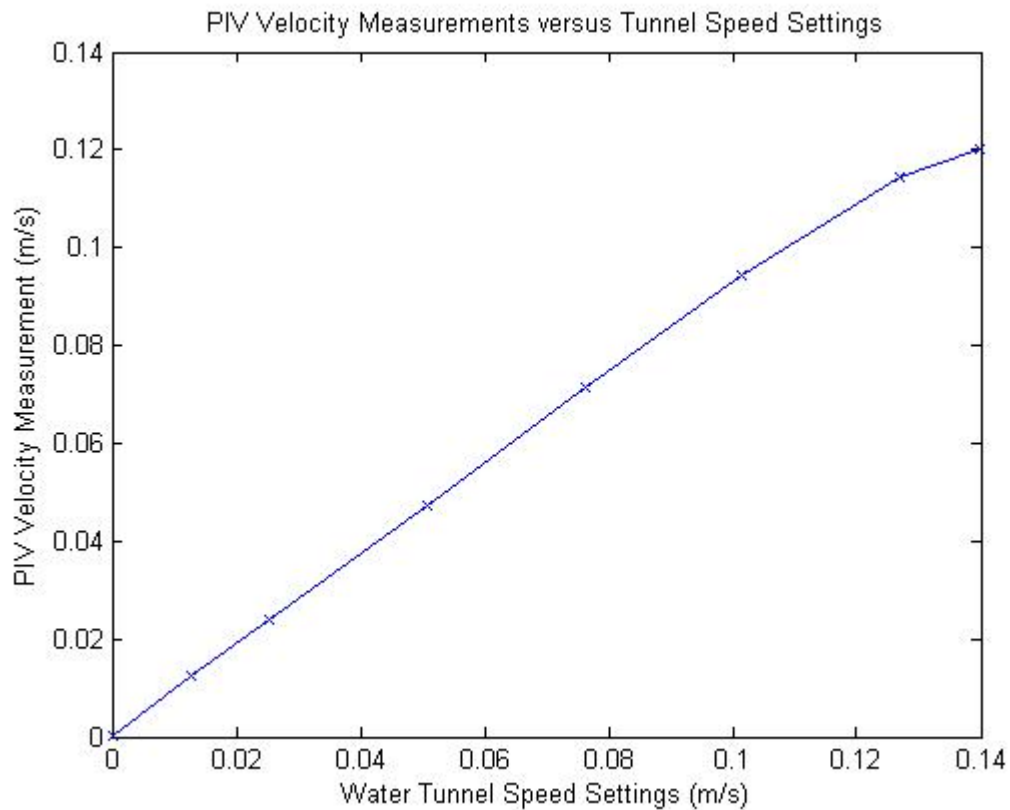


Figure 16 PIV Velocity Measurement vs. Tunnel Speed Setting

There is a consistent 6-7 % difference in the nominal tunnel speed based on the variable frequency drive setting and the velocity the PIV system measured. The data from the eight tunnel settings versus the PIV measured quantities is shown in Table 3.

Table 3 Tunnel Speed versus PIV Data

| Tunnel Speed (m/s) | PIV Measured Speed (m/s) | Standard Deviation From PIV (m/s) |
|--------------------|--------------------------|-----------------------------------|
| 0.140 | 0.120 | 0.0050 |
| 0.127 | 0.114 | 0.0033 |
| 0.102 | 0.095 | 0.0048 |
| 0.077 | 0.071 | 0.0056 |
| 0.051 | 0.047 | 0.0062 |
| 0.025 | 0.024 | 0.0028 |
| 0.013 | 0.012 | 0.0017 |
| 0 | 1.37E-05 | 0.00078 |

The tunnel speed controller was set to 0.127 m/s for all runs with the cylinders. The PIV measured velocity of 0.114 m/s was used as the free stream velocity in all the subsequent calculations.

4.2 Synthetic Jet Characteristics

In order to determine how the synthetic jet would affect the boundary layer and the wake of the cylinder, the jet was operated in quiescent conditions. The jet was operated at the conditions specified in Table 2. The parameter range was chosen to give a wide spread and because the presence of a synthetic jet could not be detected below 0.375 Hz and the Scotch–Yoke mechanism was not stable at operating frequencies above 3.5 Hz. The full stroke length of the piston was used for all the data runs. A sample of the average velocity is shown in Figure 17. The average velocity was calculated over the 75 image pairs using the Flowmap PIV software. The cylinder is located on the left side of the figure with the exit slot at right most edge of the cylinder.

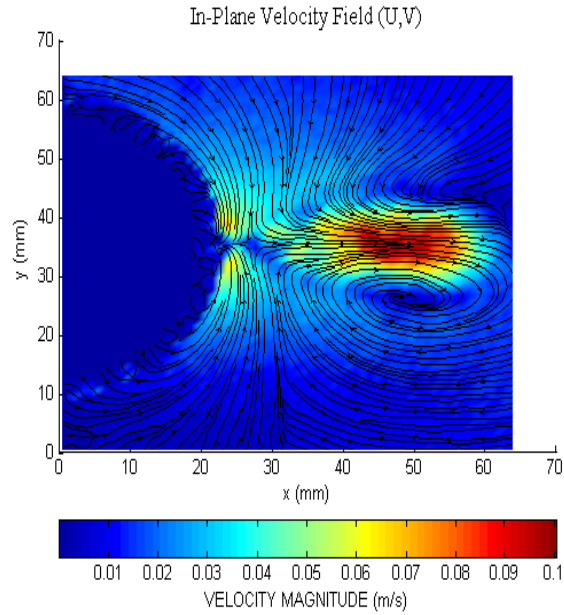


Figure 17 Average Velocity of Jet Operating at 2.5 Hz

The net effect of the counter-rotating vortices can be easily seen in Figure 17. As noted by Bera et al., the averaged velocity plot shows the superposition of alternative blowing perpendicular to the cylinder and lateral suction parallel to the wall (3). As the oscillation frequency increased the average effect of the jet becomes more pronounced. As the strength of the jet increases, the jet pulls in fluid from greater distances away from the exit, and the counter rotating vortices become stronger. The streamlines show the flow being accelerated toward the jet exit. A stagnation point is formed along the centerline of the jet due to the periodic reversal of the flow. The presence of the stagnation point shows the suction flow is confined to the region near the exit plane. As the strength of the jet increased, the stagnation point moved farther away from the jet exit, indicating that the suction flow draws in fluid from farther away from the surface of the cylinder. The average streamline velocity plots for the other jet operating frequencies can be found in Appendix A.

Figure 18 through Figure 20 show the various stages of the synthetic jet cycle. Figure 18 shows the jet during the ejection phase. The presence of the counter rotating vortices can be easily seen. The region of maximum velocity is concentrated in a small region just outside of the jet exit. Figure 19 shows that as the vortices move away from the cylinder the jet pulls additional fluid from around the cylinder with it. The flow created by the jet slows down and begins to breakup as it continues downstream from the jet exit. During the suction phase of the synthetic jet, Figure 20, fluid is drawn into the jet exit symmetrically.

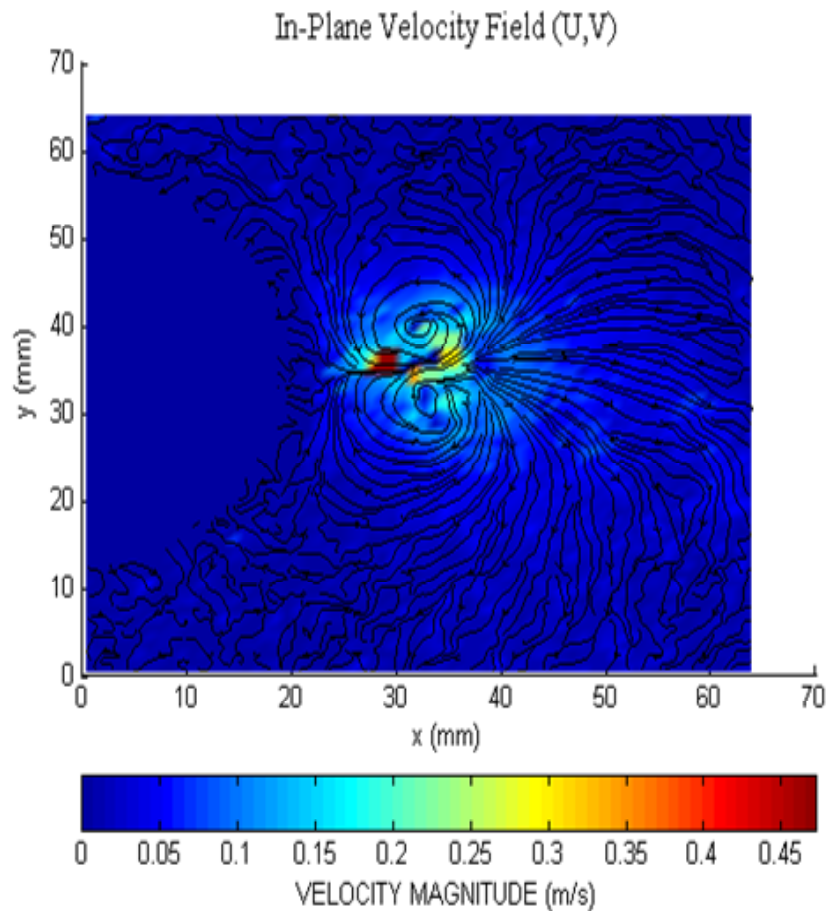


Figure 18 Synthetic Jet During Ejection at Operating 2.5 Hz

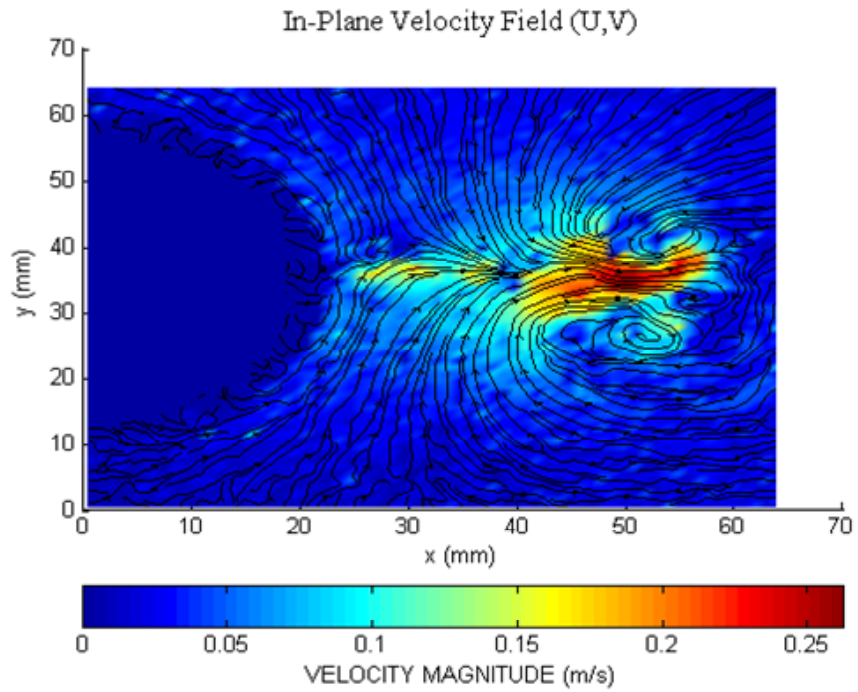


Figure 19 Synthetic Jet Post Ejection Operating at 2.5 Hz

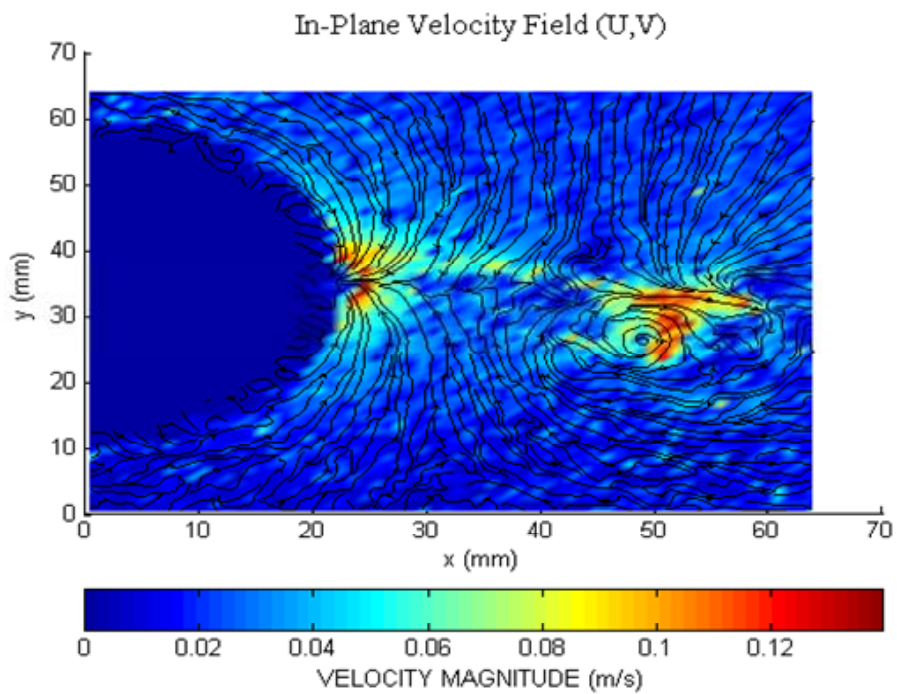


Figure 20 Synthetic Jet During Suction Operating at 2.5 Hz

4.3 Synthetic Jet Effect on Boundary Layer

Using the synthetic jet to delay separation of the boundary layer was the main objective this research. The goal was to use the jet to overcome the unfavorable pressure gradient that causes the flow to separate. As noted in Chapter 2, laminar flow separates from a cylinder between 70° and 80° . Unfortunately this could not be verified during this research effort due to a difference in the refractive index between the water and the acrylic cylinders. As a result of the refractive index the acrylic cylinders deformed the light sheet. The cylinder focused the beam to a narrow region on the upstream side of the cylinder. This phenomenon is depicted in Figure 21 with the flow moving from left to right.

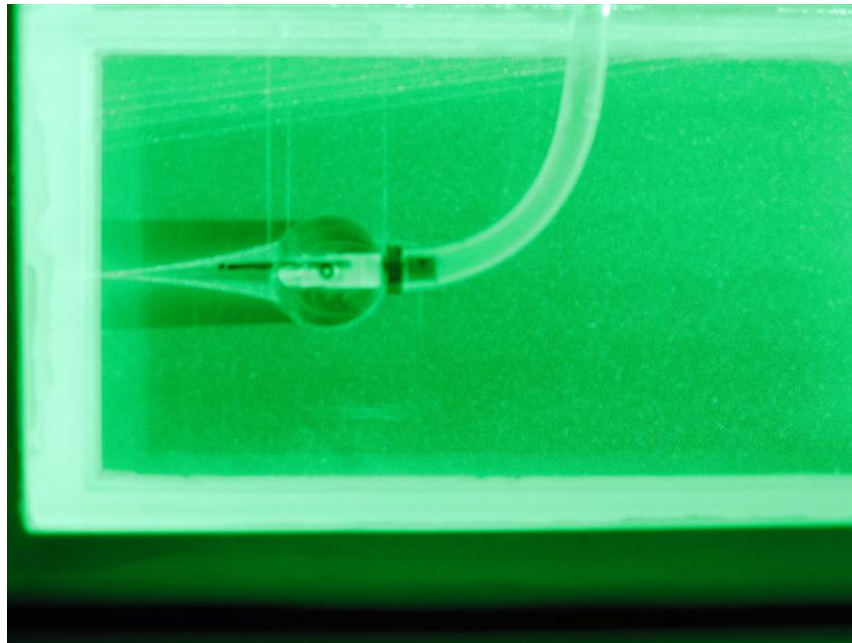


Figure 21 Laser Light Refraction

The focusing caused dark areas where reduced laser light was present on the upstream side of the cylinders causing erroneous velocity readings at this location.

The unmodified cylinder was used to act as a baseline for the effects of the synthetic jet flow around the cylinder. The Reynolds number based on cylinder diameter for the flow is $Re_D \approx 5800$, which is well within the laminar flow range. The time averaged velocity of the flow around the baseline cylinder is shown in Figure 22. The cylinder is located in the solid blue region. Based the PIV data from the baseline cylinder the flow is believed to fully separate from the cylinder at $\approx 90^\circ$ which is located at the point 27 mm along the x-axis and 29 mm along the y-axis in Figure 22. The recirculation region can be clearly be seen aft of the cylinder. The effect of the refracted laser sheet can also be seen in the figure. The velocity data along the leading of the cylinder is not consistent with laminar flow as a result of the laser light refraction.

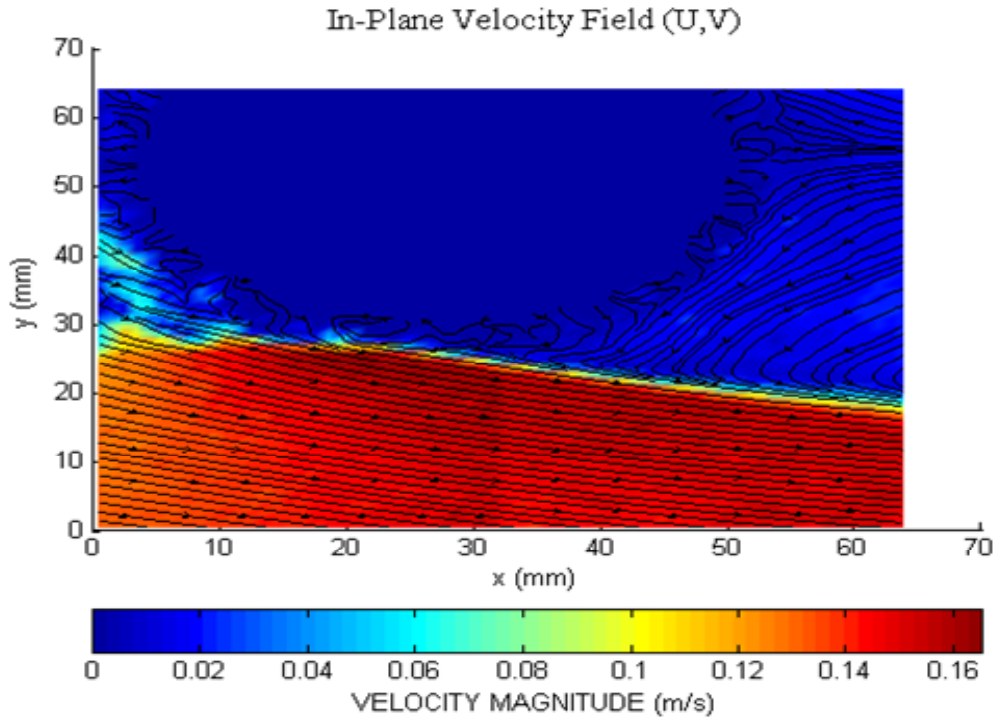


Figure 22 Streamline Velocity Plot of Baseline Cylinder

The position of the slot was varied from 0°, 45°, 70°, 90°, 110°, 135°, and 180° and the jet was operated at varying frequencies for the same piston stroke length which resulted in different momentum blowing coefficients. The averaged PIV data was used to generate streamline velocity plots as well as velocity profile plots. The velocity profiles were examined at $\frac{3}{4}$ diameter location on the cylinder. Velocity profiles were created to show the effect on the flow by changing the momentum coefficient and jet exit position.

Trends appeared as a result of examining the velocity plots and the velocity profiles that related the jet exit location, momentum transfer coefficient, and the effect on the boundary layer of the cylinder. Depending on the location of the jet exit and momentum coefficient the effect can be favorable, unfavorable or indifferent. At the 0°, 135°, and 180° jet locations the velocity profiles showed that as the oscillation frequency of the jet increased the velocity profiles were positively affected. The apparent separation point moved further aft on the cylinder as momentum coefficient was increased. The 135° jet exit slot location with the momentum coefficient ($C_{\mu jrms}$) of 3.11 had the most profound effect on the separation point on with the flow staying attached up to the exit slot. As a result of the laser light being refracted by the cylinder effect of the jet at the 0° and 45° was not able to be as thoroughly studied as the rest of the exit slot locations. The effect of frequency variation on the 135° location is shown in Figure 23.

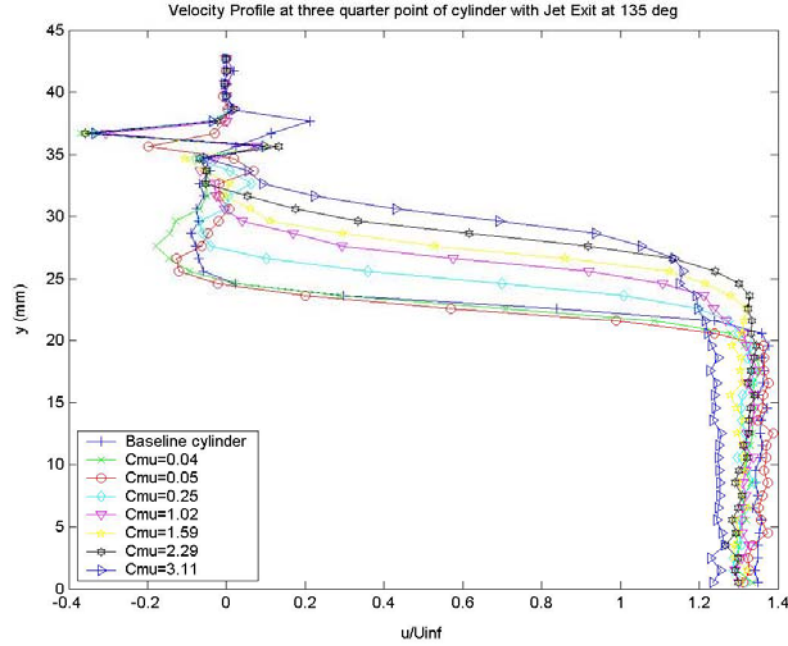


Figure 23 Velocity Profiles at 3/4 Diameter, Jet at 135 deg and Varying C_{μ}

At the 45° , 70° , 90° , 110° jet locations the relationship between the momentum coefficient and a favorable velocity profile was not linear. At these exit locations the increase in the momentum coefficient created a favorable velocity profile and delayed separation of the boundary up to a point. As the momentum coefficient was increased beyond this point the effect on the velocity profiles was not necessarily worse than the baseline case, but was suboptimal. At the 45° and 70° slot locations the jet produced a favorable effect on the flow up to a $C_{\mu_{jrms}}$ of 1.02. The effect of frequency variation when the jet exit is located at 70° is shown in Figure 24.

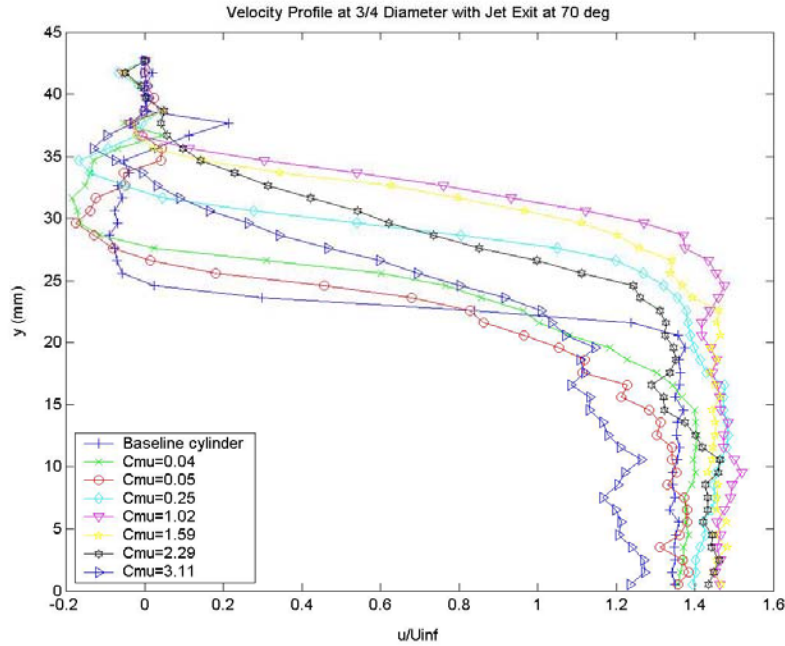


Figure 24 Velocity Profile at 3/4 Diameters with Jet Exit at 70 with Varying Cmu

The 90° and 110° locations had the greatest effect on the flow when the jet was operated at $C_{\mu jms} = 0.25$. Figure 25 shows how changing the oscillatory momentum blowing coefficient affects the velocity profiles at the $\frac{3}{4}$ diameter point on the cylinder. Beyond this value, the net effect of the jet was to vector the flow away from the cylinder. The increase in reverse flow during the suction phase of the jet was enough to overcome the flow around the cylinder. This is shown in Figure 26 and Figure 27. The 110° exit location cases behaved similarly to the 90° ones.

The velocity profiles of the 0, 45, 90, and 180 jet exit locations are located in Appendix C.1.

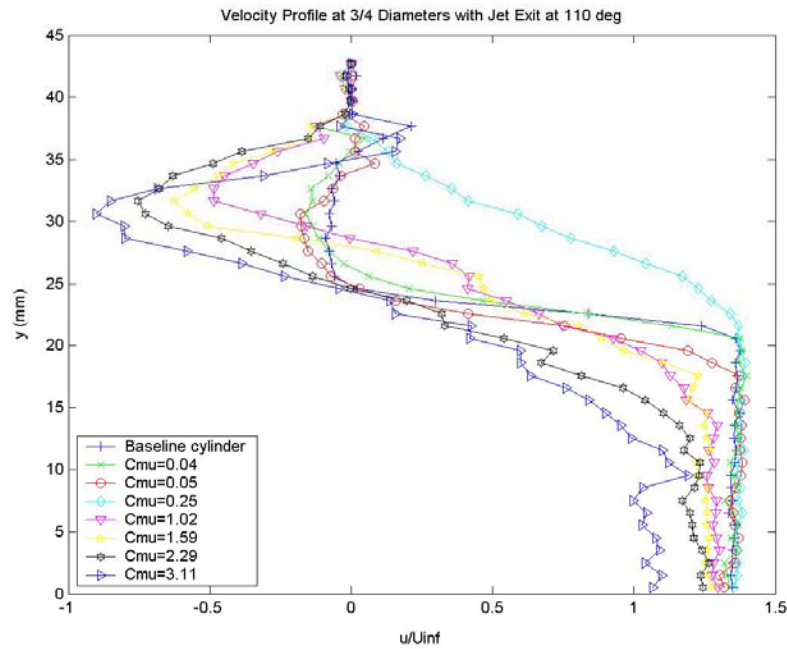


Figure 25 Velocity Profile at 3/4 Diameter with Jet Exit at 110 deg with Varying Cmu

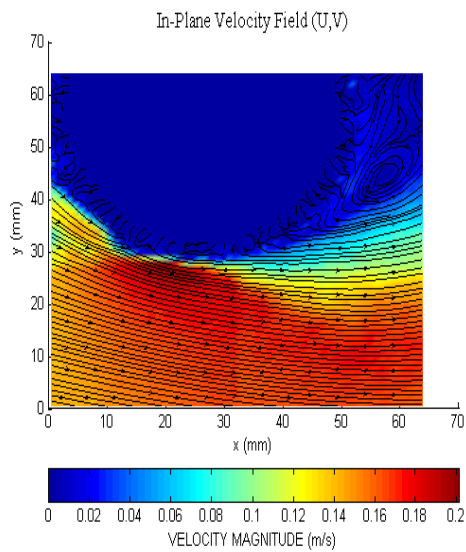


Figure 26 Jet at 90 deg with Cmu=0.25

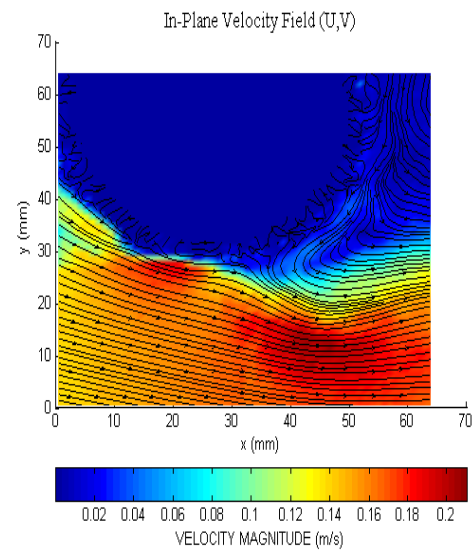


Figure 27 jet at 90 deg with Cmu=1.02

In addition, the velocity profiles were examined to determine the effect of changing jet exit position and holding $C_{\mu rms}$. The velocity profiles were calculated at $3/4$ diameter position on the cylinder. Figure 28 shows the effect of changing the jet location while holding $C_{\mu rms}$ constant at 0.05. The 90° slot position had the greatest positive effect on the velocity profile. The remaining jet locations at this setting did not have much of an effect on the flow compared to the baseline cylinder profile. The velocity profiles for $C_{\mu rms}=0.04$ are shown in appendix C because they are very similar to 0.05 profiles.

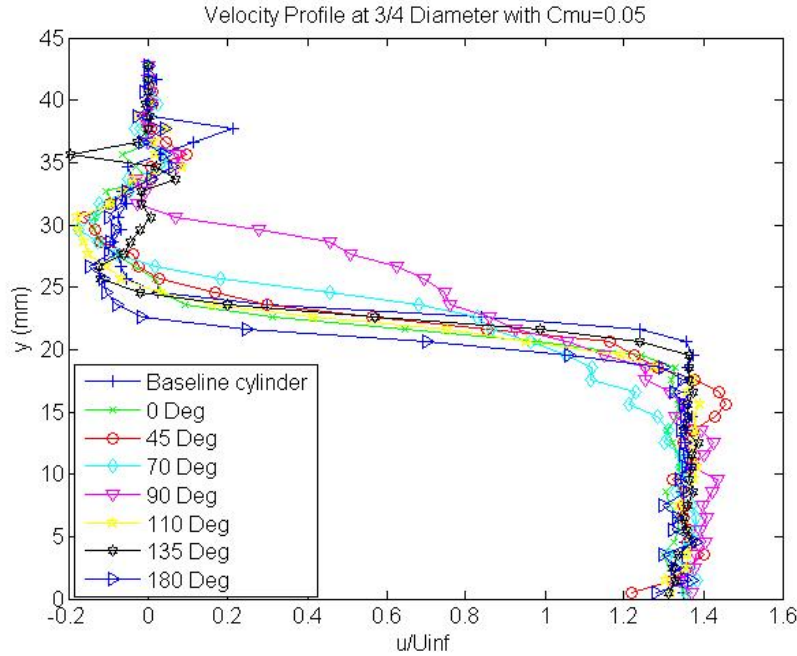


Figure 28 Velocity Profiles with $C_{\mu}=0.05$ and Varying Jet Location

When $C_{\mu rms}$ is increase to 0.25 the 45° , 70° , 90° and 110° jet locations the velocity of the flow reached a higher velocity closer to the cylinder than the baseline case. The velocity profiles for the 0° and the 135° locations were nearly identical. The 180°

location had no effect on the flow compared to the baseline cylinder. The velocity profiles for $C_{\mu jrms}=0.25$ are shown in Figure 29.

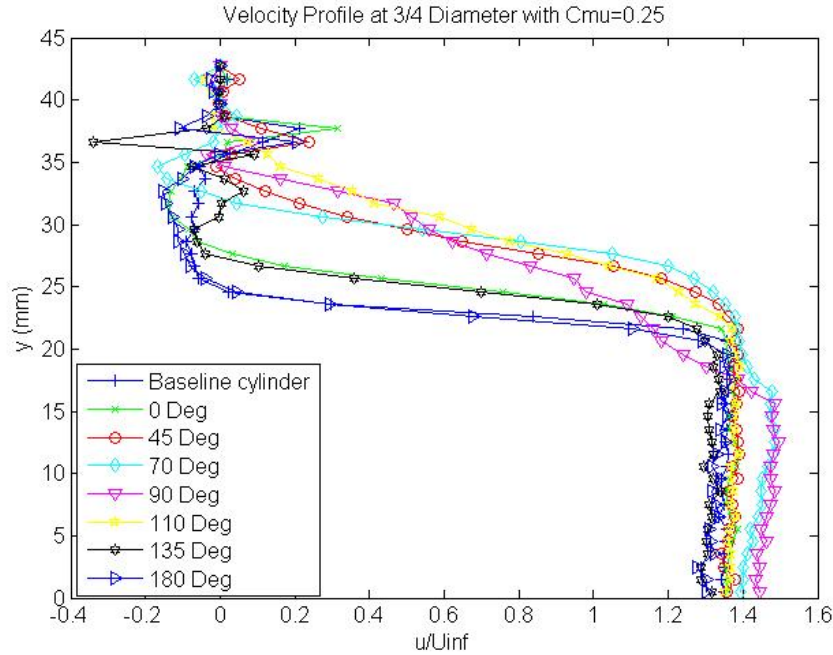


Figure 29 Velocity Profiles with $C_{\mu}=0.25$ and Varying Jet Location

At $C_{\mu jrms}=1.59$ resulted in a large spread between the jet exit locations. The 70° had the greatest positive effect on the flow by adding higher momentum fluid closer to the cylinder than the other cases. The 45° and 135° locations also produced a substantial effect on the velocity profile. The 110° case resulted in negative velocity near the cylinder because fluid downstream of the jet is drawn into the jet orifice. When the jet is located at 90° , its greatest effect on the flow is away from the cylinder resulting in a peak velocity of 1.75 times greater than the free stream velocity at a distance of 30 mm from the surface of the cylinder. The velocity profiles for $C_{\mu jrms}=1.02$ are shown in Figure 30. The velocity profiles for the $C_{\mu jrms}=1.59$ are shown in Figure 65 which is located in

appendix C which are similar to the $C_{\mu jrms}=1.02$ profiles. These effects are further illustrated in Figure 31, which shows the average velocity of the fluid around the cylinder at $C_{\mu jrms}=1.02$ and the jet location varying from 70° to 90° to 110° .

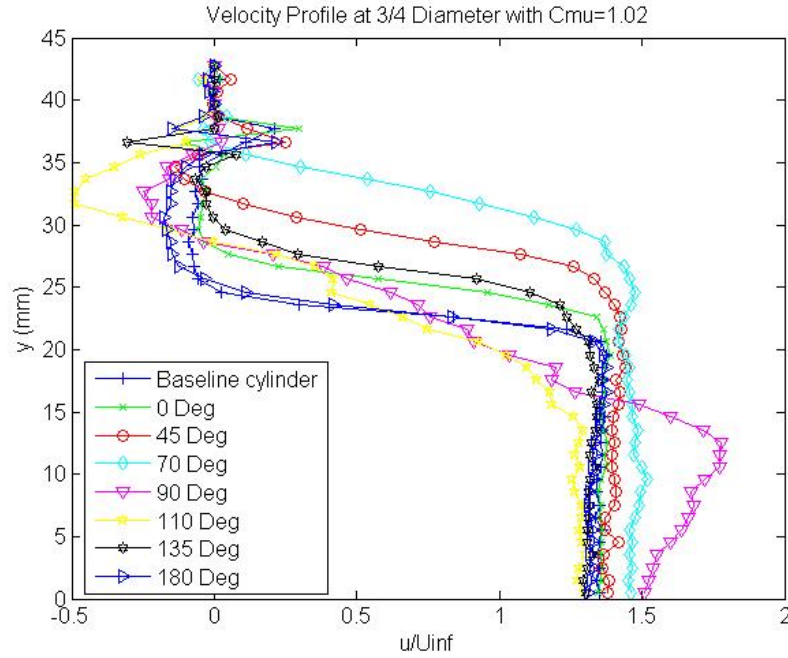


Figure 30 Velocity Profiles with $C_{\mu}=1.02$ and Varying Jet Location

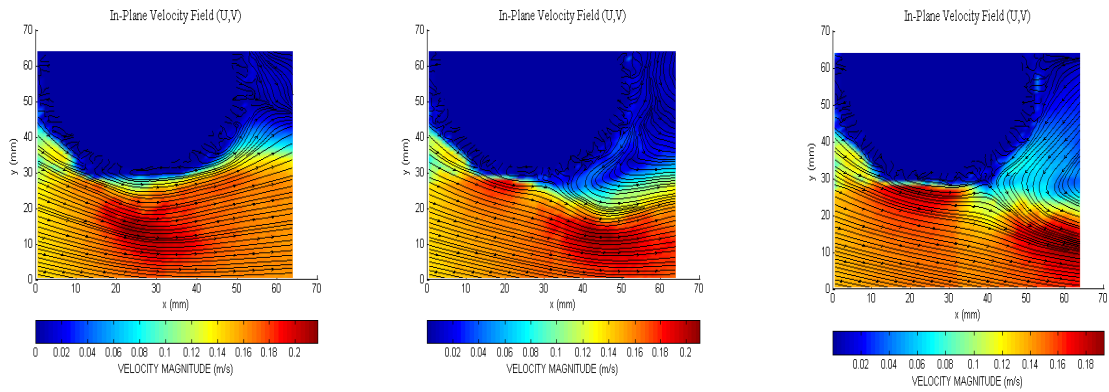


Figure 31 Average Streamline Velocity for $C_{\mu}=1.02$ at 70 deg, 90 deg, and 110 deg

The 45 and 135° locations had the greatest positive effect on the velocity profile at the highest $C_{\mu rms}$ setting of 3.11. The 0 and 180 locations produced nearly identical results. The negative velocity produced by the action of the jet at the 110 location is more pronounced at $C_{\mu rms}=3.11$. The peak velocity of the 90 location is farther away from the cylinder than the $C_{\mu rms}=1.02$, but the peak velocity is less than the $C_{\mu rms}=1.02$. The velocity profiles for $C_{\mu rms}=3.11$ are shown in Figure 32. Due to similarity, the velocity profiles for $C_{\mu rms}=2.29$ are in Figure 66 which is located in appendix C.

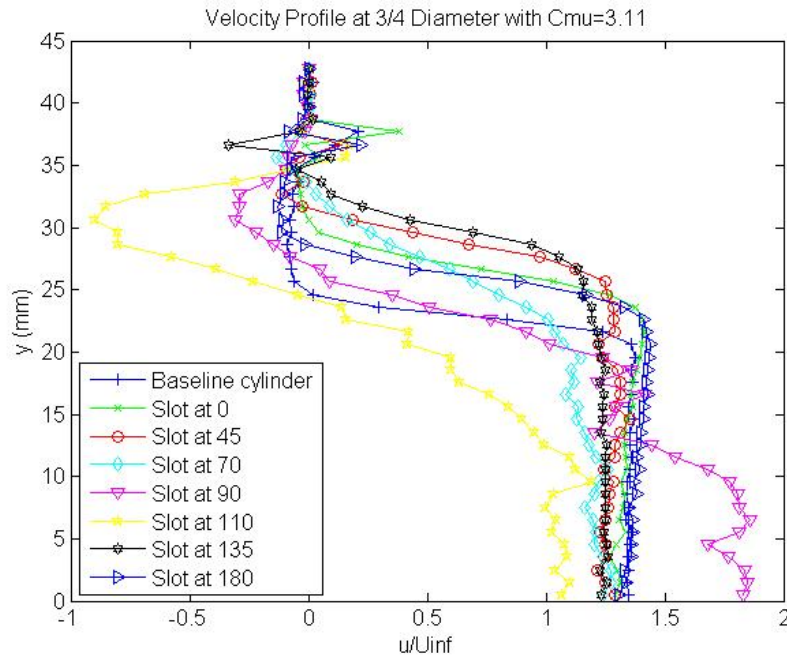


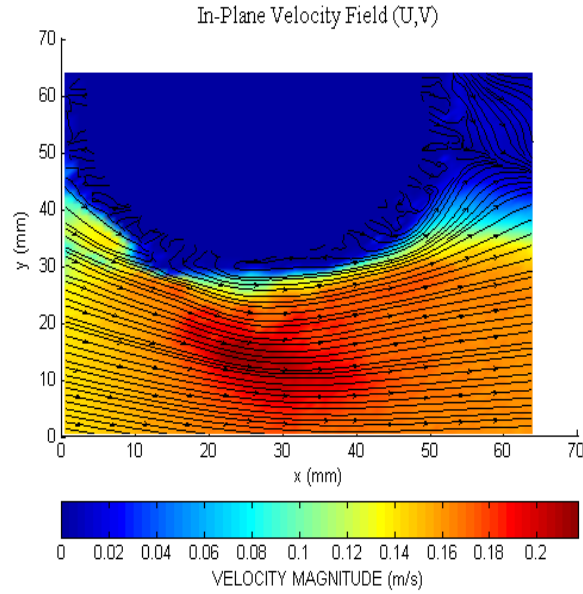
Figure 32 Velocity Profiles with $C_{\mu}=3.11$ and Varying Jet Location

Based on the comparisons of jet angle and momentum coefficient three cases were chosen for further study to determine how they affected the flow around the cylinder. The three cases chosen for additional examination were 70° at 2 Hz, 110° at 1 Hz and 135° at 3.5 Hz. The three cases that were chosen for further study are shown in Table 4 with the pertinent parameters.

Table 4 Case Parameters

| | Case 1 | Case 2 | Case 3 |
|----------------------------|--------|--------|--------|
| Jet Exit Position | 70° | 110° | 135° |
| Oscillation Frequency (Hz) | 2 | 1 | 3.5 |
| RMS of Exit Velocity (m/s) | 0.46 | 0.23 | 0.81 |
| $C_{\mu_{rms}}$ | 1.02 | 0.25 | 3.11 |
| F^+ | 0.90 | 0.45 | 1.57 |
| F | 4.47 | 2.24 | 7.83 |

The streamline velocity plots for each test point are shown in Figure 33 through Figure 35.

**Figure 33 Average Streamline Velocity Plot of Case 1**

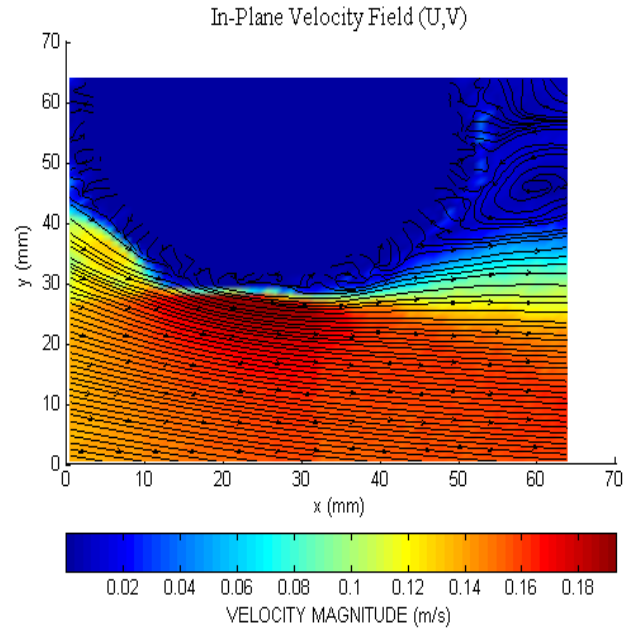


Figure 34 Average Streamline Velocity Plot of Case 2

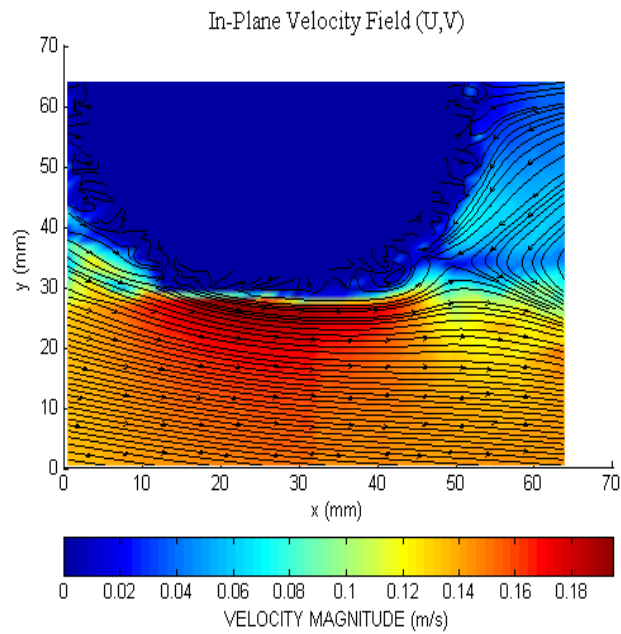


Figure 35 Average Streamline Velocity Plot of Case 3

All three cases imparted sufficient velocity to the boundary layer of the flow to overcome the adverse pressure gradient. Based on Figure 33 through Figure 35, cases 1 and 3 had a greater effect than case 2 in keeping the boundary layer attached and delaying

separation. In order to examine the flow more closely velocity profiles were generated at the $\frac{1}{2}$ diameter, $\frac{3}{4}$ diameter, and 1 diameter from the upstream side of the cylinder. The velocity profile plots have the displacement on the ordinate. The highest point data point on the profiles corresponds to the bottom of the cylinder for the $\frac{1}{2}$ diameter and $\frac{3}{4}$ diameter plots. The highest point on the 1 diameter velocity profiles corresponds to the highest point from the PIV images. The abscissa is the non-dimensionalized velocity. The actual velocity, u , derived from the PIV data was divided by the free stream velocity, U_∞ which was determined from PIV data without the cylinder in the tunnel. Some of the non-dimensionalized velocities will be greater than unity due to the non-dimensionalization routine. All three test cases had a favorable effect on the streamwise average velocity profile when compared to the baseline case. The velocity profiles at the $\frac{1}{2}$ diameter location are shown in Figure 36 with the standard deviations shown in Figure 37. There is little difference in the velocity profiles at the $\frac{1}{2}$ diameter points between cases 2 and 3, while case 1 behaves quite differently. The velocity profiles of cases 2 and 3 approach the values of the baseline case as the distance away from the cylinder increases. While the velocity profile for case 1 reaches its maximum value further away from the cylinder. When the standard deviations of the velocity are examined it shows the variation of the velocity at each point over the 75 image pairs. The standard deviation of test case 1 is orders of magnitude larger than cases 2 and 3. The standard deviation of cases 2 and 3 are of the same order of magnitude. The large spread of the standard deviation cases 1 is due to the vortices generated by the synthetic jet. The standard deviations of the velocities were calculated by the Flowmap PIV software.

At $\frac{3}{4}$ diameters and 1 diameter that effects of the jet are more pronounced on the velocity profiles with test cases 1 and 2 having the greatest effect. The $\frac{3}{4}$ and 1 diameter velocity profiles and the standard deviations of each are shown in Figure 38, Figure 39, Figure 40, and Figure 41.

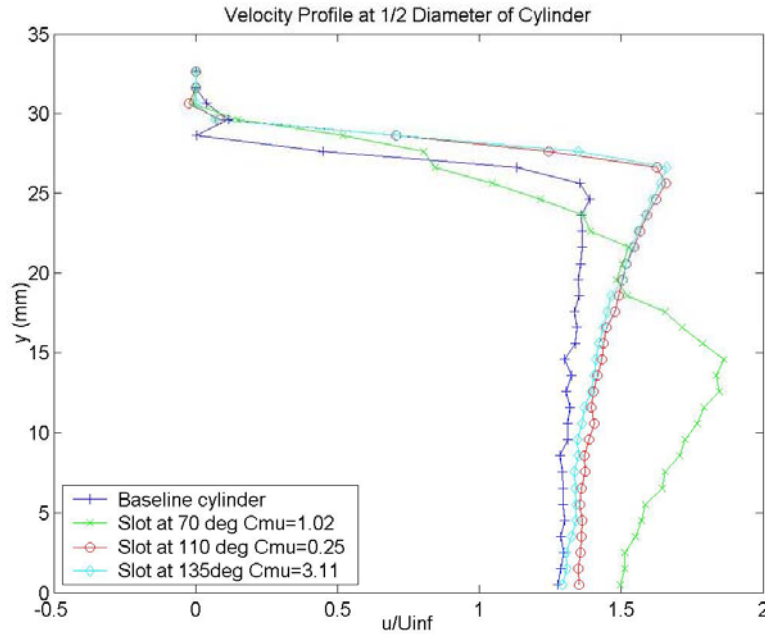


Figure 36 Average Velocity Profile at $\frac{1}{2}$ Diameter of Cylinder

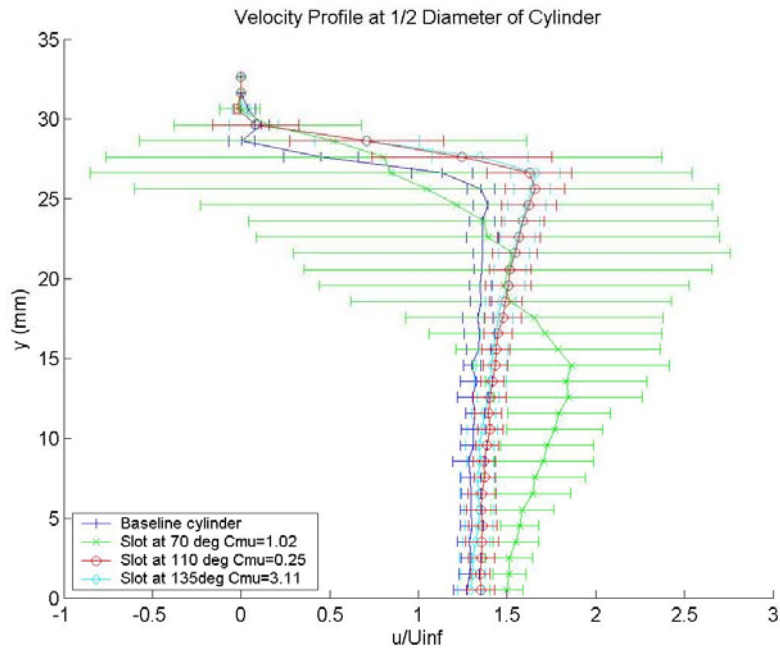


Figure 37 Average Velocity Profile with Standard Deviations at 1/2 Diameter

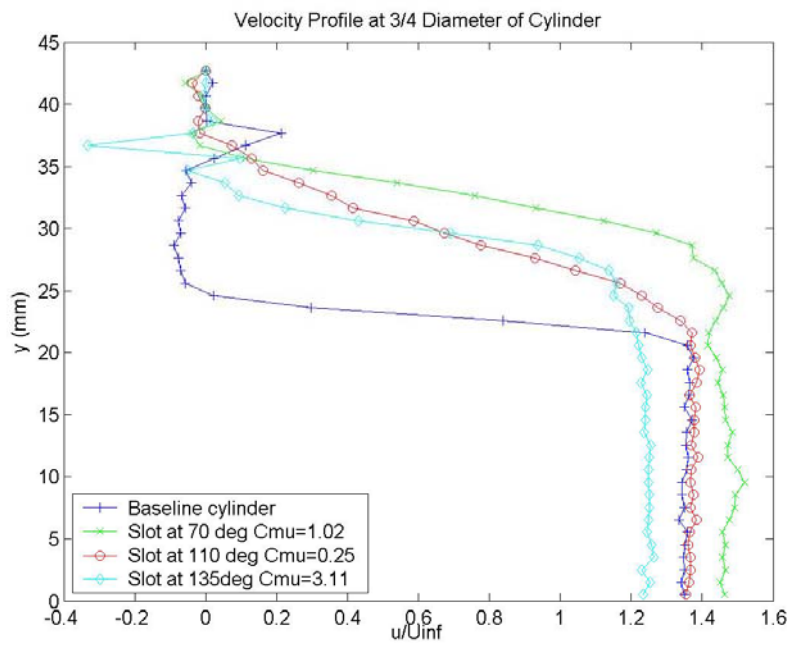


Figure 38 Average Velocity Profile at 3/4 Diameter

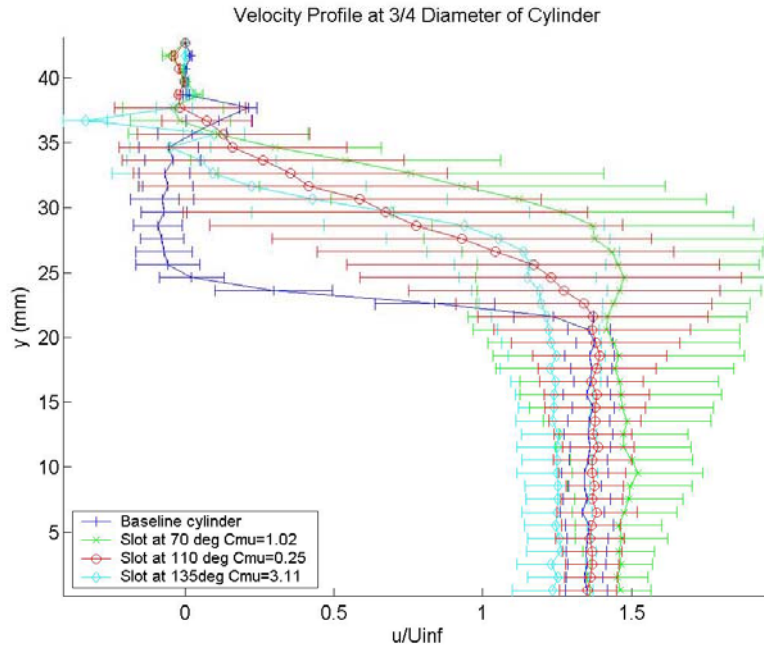


Figure 39 Average Velocity Profile with Standard Deviation at 3/4 Diameter

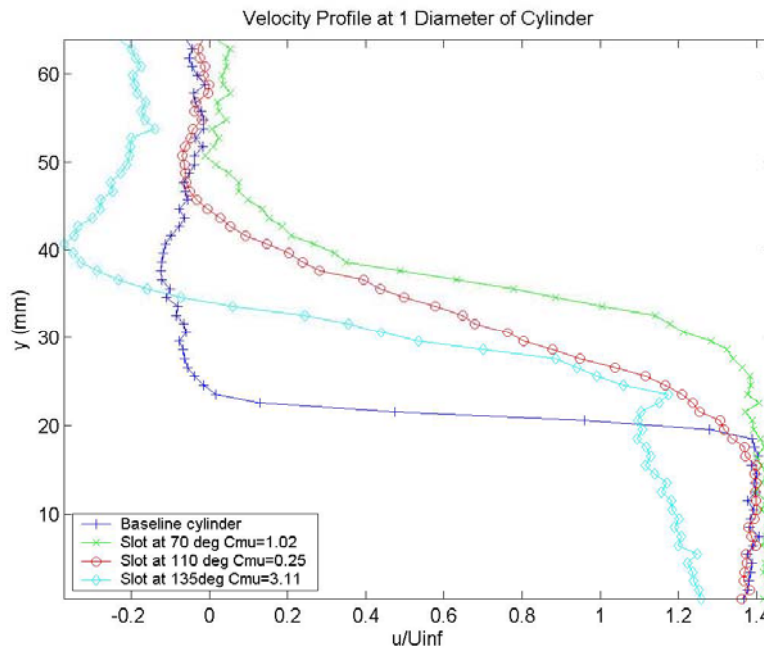


Figure 40 Average Velocity Profile at 1 Diameter

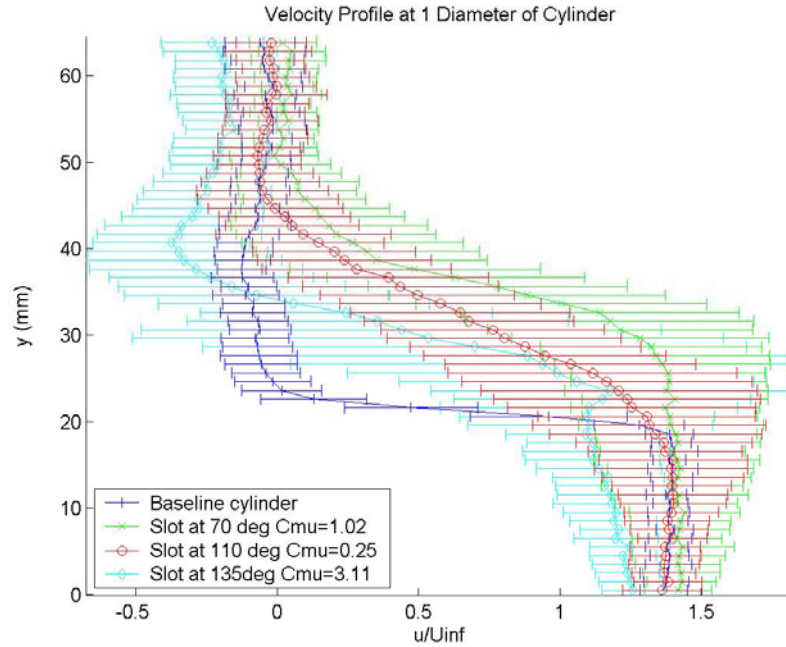


Figure 41 Average Velocity Profile with Standard Deviations at 1 Diameter

4.4 Synthetic Jet Control Mechanisms

4.4.1 Case 1 Control Mechanism

Upon careful examination of the flows the control mechanism of the three cases was be observed. In case 1, the interaction of the jet with the cross flow produced vortices that were shed downstream. The vortices caused the mixing of the higher momentum flow outside of the boundary with the slower flow of the boundary layer. The added momentum imparted to the flow was great enough for the flow to overcome the adverse pressure gradient and keep the boundary layer attached well beyond the uncontrolled baseline case.

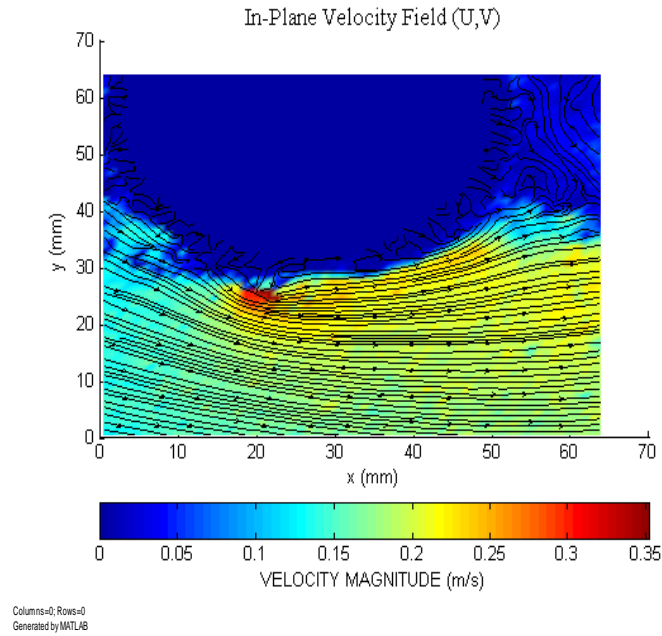


Figure 42 Ejection Phase of Jet

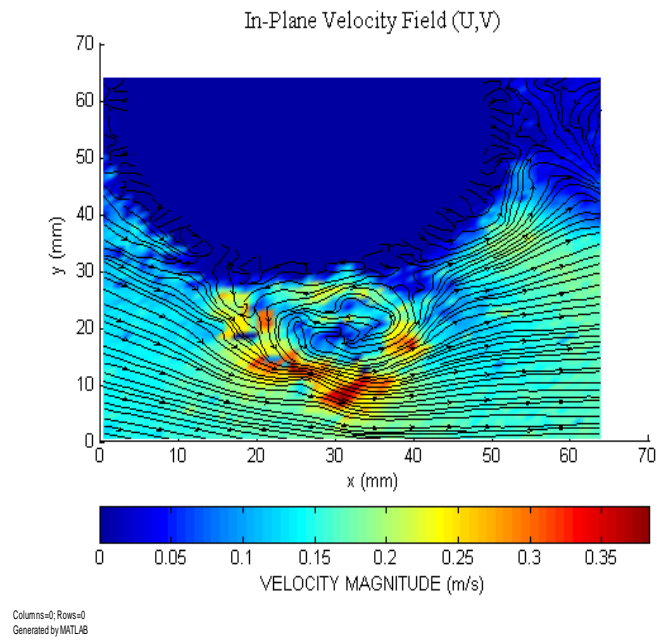


Figure 43 Vortex Mixing

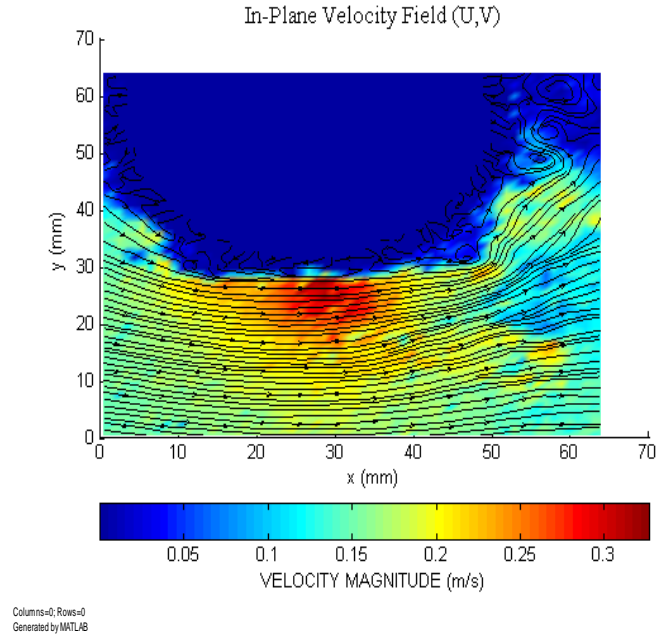


Figure 44 Jet After Vortex Shedding

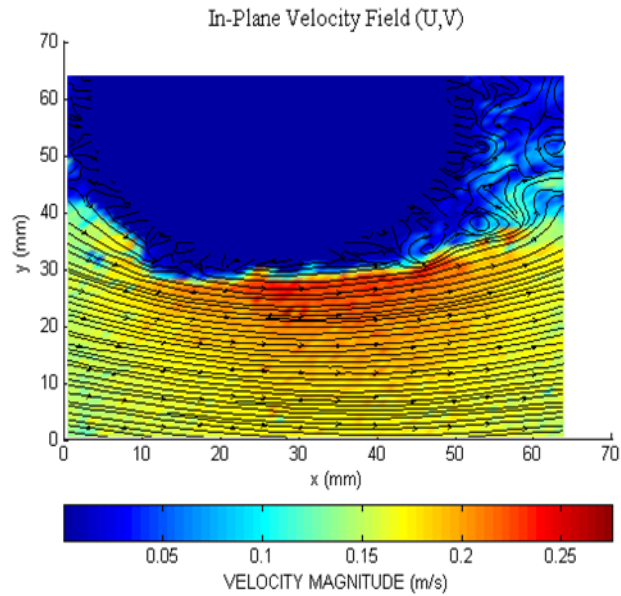


Figure 45 Suction Phase of Jet

Figure 42 through Figure 45 show the development of the synthetic jet for test case 1. In Figure 42 the jet is ejecting high momentum fluid into the boundary layer. Figure 43 shows the mixing of the higher momentum flow outside of the boundary layer with the

boundary layer. Areas of the imparted high velocity fluid can be seen in Figure 44 and Figure 45.

4.4.2 Case 2 and Case 3 Control Mechanism

The control mechanism for case 2 and 3 utilizes the suction phase of the synthetic jet cycle to keep the flow attached to the cylinder more than the ejection phase. The suction phase of the synthetic jet cycle causes the flow close to the surface of the cylinder to be accelerated toward the jet exit. During the ejection phase of the cycle fluid expelled along the center line of the jet causing the flow to separate at the jet exit location. The stages of the case 2 synthetic jet are located in Appendix B and the stages of the case 3 synthetic jet are shown in Figure 46 and Figure 47

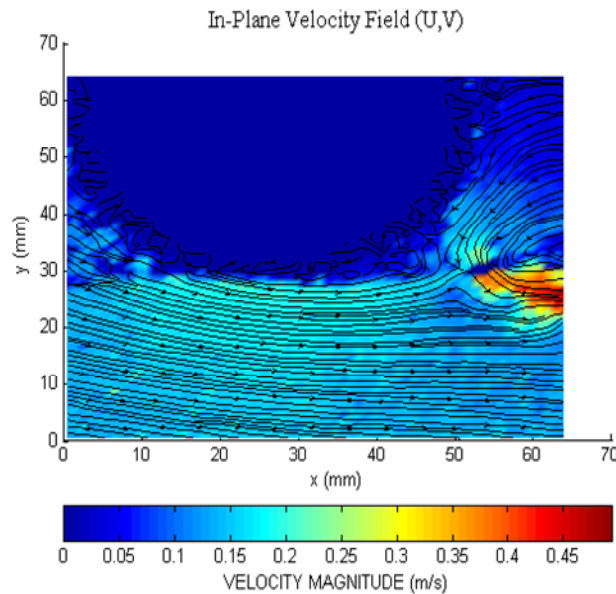


Figure 46 Ejection Phase of Case 3 Synthetic Jet

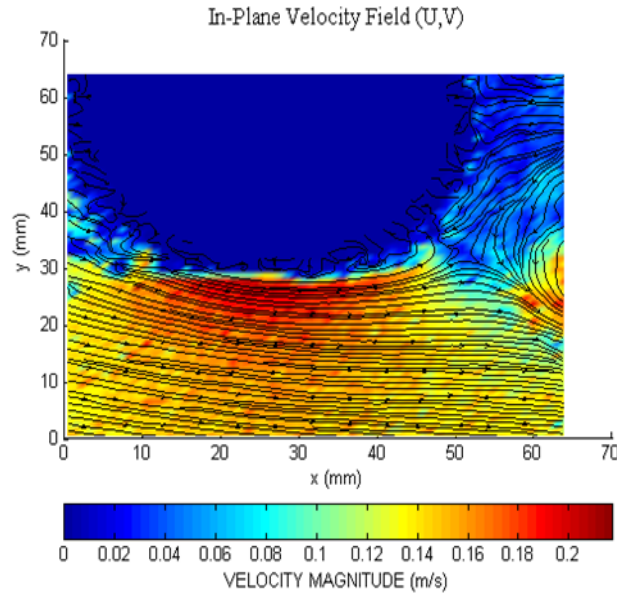


Figure 47 Suction Phase of Case 3 Synthetic Jet

Based on the streamline velocity plots and the velocity profiles case 1 does the most effective job in keeping the boundary layer of the flow around the cylinder attached. The flow stays attached to approximately 140°

4.5 Synthetic Jet Effect on Wake of Cylinder

The effect the three test settings had on the wake of the cylinder was also examined to gain additional insight on how the synthetic jet affects the flow around the cylinder. The goal of examining the wake of the cylinder is to determine the change in momentum deficient caused by the action of the jets. Figure 48 shows the average velocity plot of the baseline flow. The cylinder is located on the left side of the figure with the horizontal centerline of the cylinder at the 150mm mark. The wake is characterized by two symmetric recirculation regions. The wake of the cylinder extends several diameters downstream and does not reach U_∞ in the test section of the tunnel.

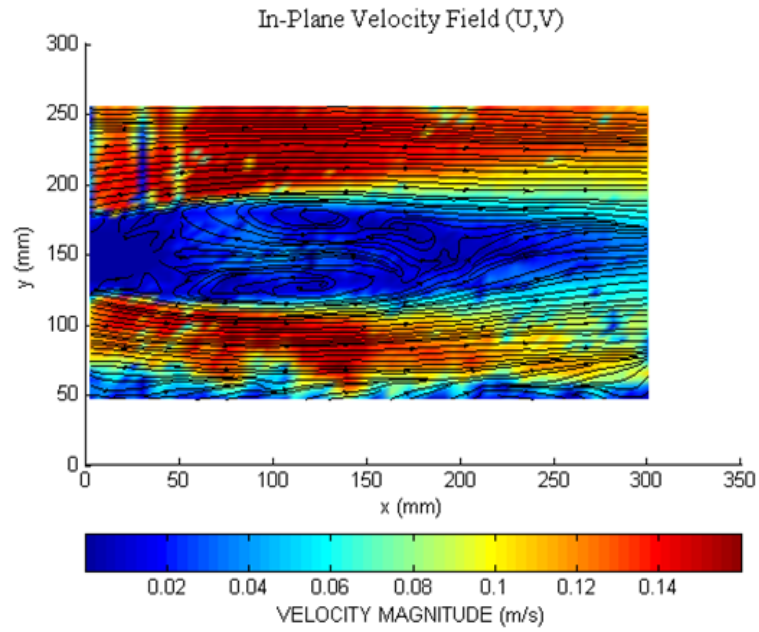


Figure 48 Far Field Average Streamline Velocity Plot of Baseline Cylinder

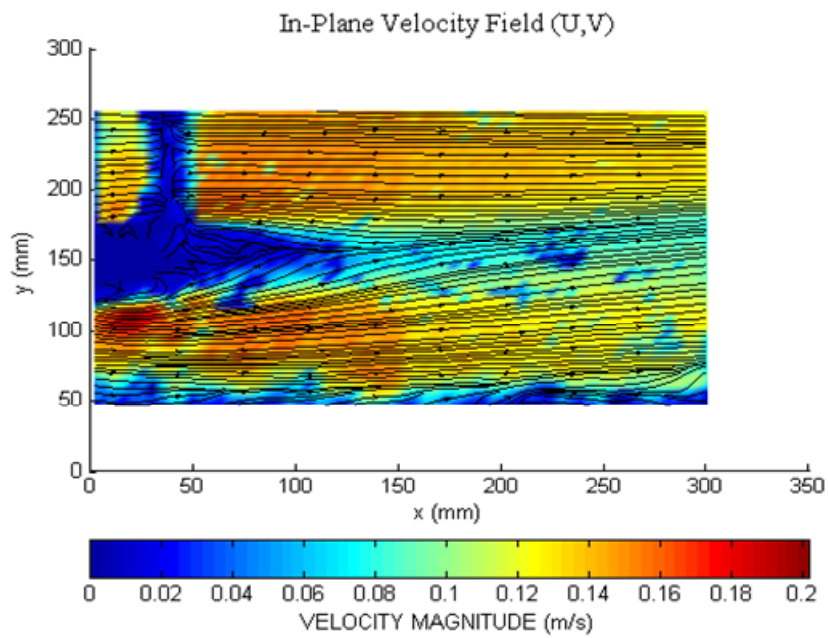


Figure 49 Case 1 Far Field Average Streamline Velocity Plot

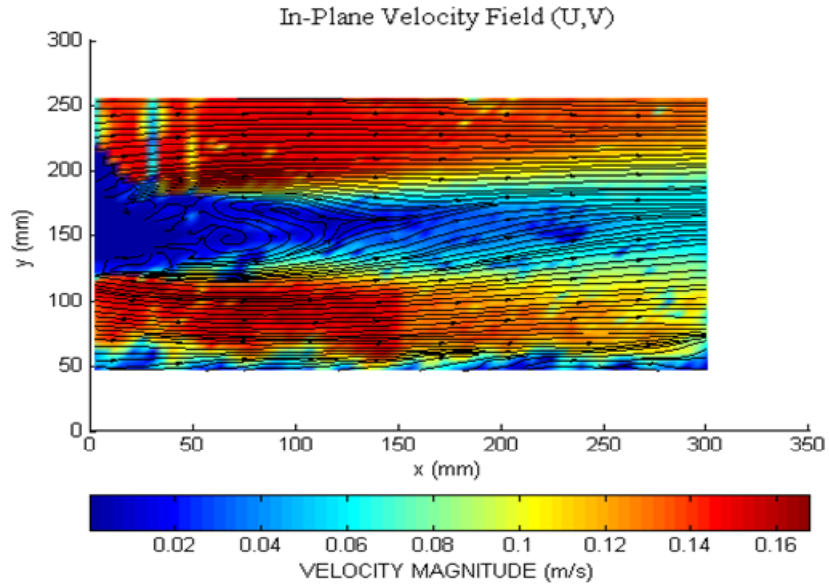


Figure 50 Case 2 Far Field Average Streamline Velocity Plot

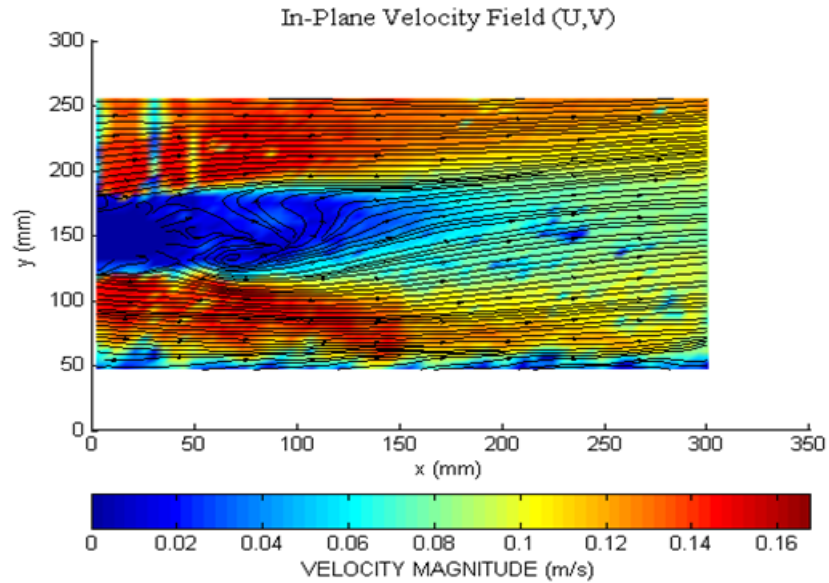


Figure 51 Case 3 Far Field Average Streamline Velocity Plot

When the three test cases and the baseline test are examined the effect of the synthetic jet is readily apparent. The streamline velocity profiles for the test cases are shown in Figure 49, Figure 50, and Figure 51. The wake of the test cases is no longer

symmetric about the horizontal centerline axis of the cylinder. The action of the jet on the lower side of the cylinder and the subsequent vortex shedding cause the streamlines of the wake of the cylinder to be steered toward the wake the uncontrolled side of the cylinder. Each of the three cases decreases the length of the cylinder's wake.

Velocity profiles were generated at 1, 3, and 5 diameters aft of the cylinder. From the velocity profiles the momentum thickness of the wake was calculated. The velocity profile 1 diameter aft of the cylinder is shown in Figure 52. The velocity profile plots at 3 and 5 diameters aft of the cylinders are location in Appendix C.

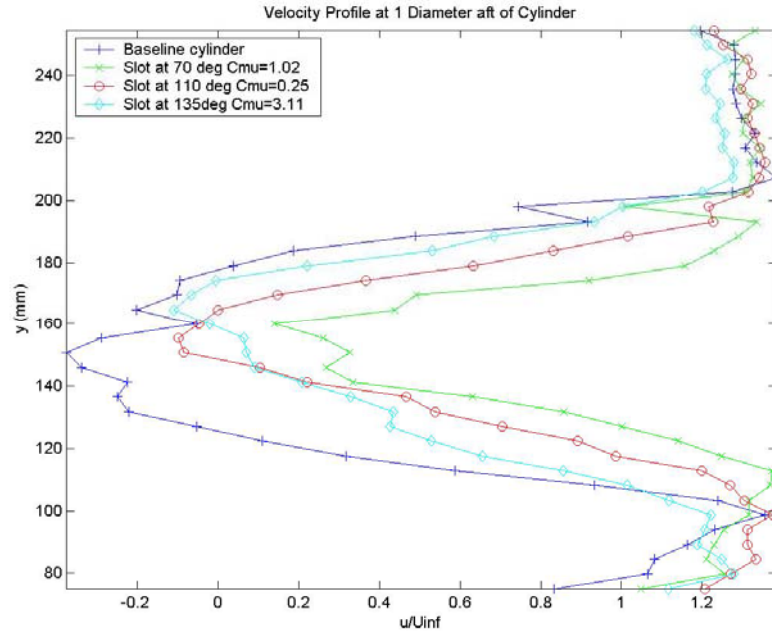


Figure 52 Velocity Profile at 1 Diameter Aft of Cylinder

The momentum thickness of the wake was calculated using (18).

$$\theta_{\text{wake}} = \int_{-\infty}^{\infty} \frac{\Delta u}{U_{\infty}} \left(1 - \frac{\Delta u}{U_{\infty}} \right) dy \quad (14)$$

Table 5 Momentum Thickness of Cylinder Wake

| Measurement Location | Baseline | Case 1 | Case 2 | Case 3 |
|----------------------|----------|--------|--------|--------|
| 1 Diameter | -34.09 | -3.5 | -12.39 | -18.95 |
| 3 Diameters | -24.88 | -3.06 | -13.37 | -10.52 |
| 5 Diameters | -22.91 | -5.14 | -15.41 | -11.14 |

The limits of the integration used for the calculations were the bottom and top of the test section instead of $-\infty$ and ∞ . Δu is the difference in the flow velocity, u , and the free stream velocity, U_∞ . Based on the data in Table 5, case 1 condition had the greatest impact on the momentum thickness of the wake, decreasing the momentum deficit by 77-88% when compared to the baseline case. Case 2 reduced the momentum thickness by 33-62%. The momentum thickness of case 3 was 44-57% less than the baseline case.

Chapter 5. Conclusions and Recommendations

5.1 Conclusions

The main objective of the research was to find a combination of jet exit location and operating parameters that would create favorable conditions to delay the separation of the boundary layer over a circular cylinder in cross flow with a PIV system. The synthetic jet was able to delay boundary layer separation over a wide range of angles and operating parameters. As the angle of the jet relative to the free stream approached 90° , the value of oscillatory momentum coefficient required to delay boundary layer separation decreased. At the points furthest from the uncontrolled separation point, a high oscillatory momentum coefficient resulted in delayed boundary layer separation. The optimum location and operating parameters were determined to be at jet exit location of 70° with a momentum blowing coefficient of 1.02. At this test condition separation was delayed from $\sim 90^\circ$ to $\sim 140^\circ$ and the momentum thickness was reduced by 77-88%.

5.2 Recommendations

In order to gain additional understanding of the behavior of the synthetic jet in cross flow of the important parameters that affect the synthetic jets interaction with the crossflow, the stroke length the piston needs to be varied in order to decouple the oscillatory momentum coefficient from the non-dimensional excitation frequency. The PIV system needs to be phase locked with the synthetic jet. This will allow repeated images to be taken at the same stage of the synthetic jet cycle.

The out of the image plane flow was not measured because only one PIV camera was used. The second PIV camera needs to be setup to gather 3-D PIV data to examine the three dimensional structure of the synthetic jet in quiescent conditions and in the presence of crossflow.

In order to improve upon the results of this research project, the laser refraction and reflection problems must be overcome. One possible solution is to add an additional viewing window on the bottom of the test section and aim the laser light sheet through the new window. A more non-intrusive way is to try to use refractive index matching. This process involves changing the refractive index of the fluid to match the index of the model. The laser reflection problem can be alleviated by using laser induced fluorescence (LIF). In LIF, particles are added to the flow that fluoresce when hit with laser light. The light wavelength that is emitted by the particles is different from the wavelength of the laser. A filter can be placed over the lens of the camera to allow only the fluorescing wavelength through.

Appendix A. Streamline Velocity Figures

The streamline velocity figures in this section are a continuation of the material presented in Chapter 4 Section 2.

A1. Average Streamline Velocity in Quiescent Conditions

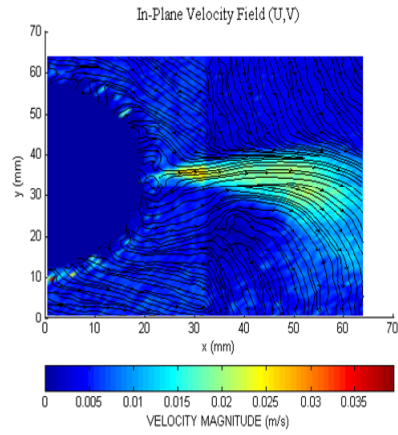


Figure 53 Average Velocity at .375 Hz

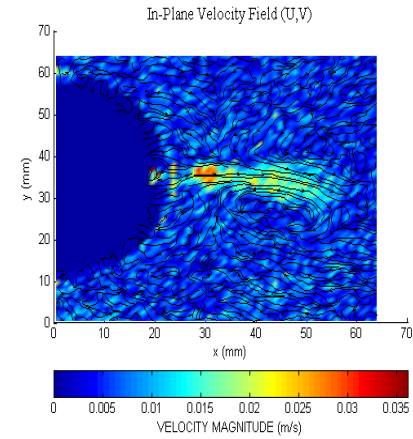


Figure 54 Average Velocity at 0.45 Hz

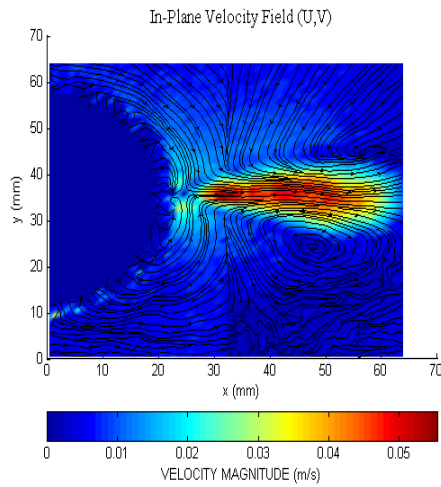


Figure 55 Average Velocity at 1 Hz

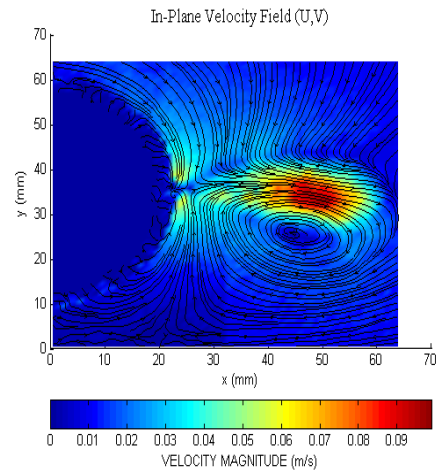


Figure 56 Average Velocity at 2 Hz

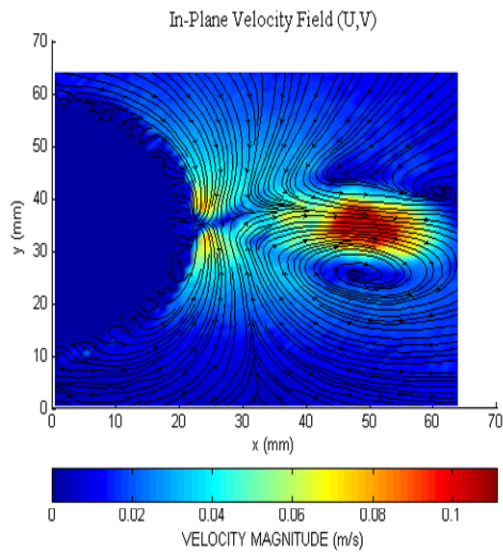


Figure 57 Average Velocity at 3 Hz

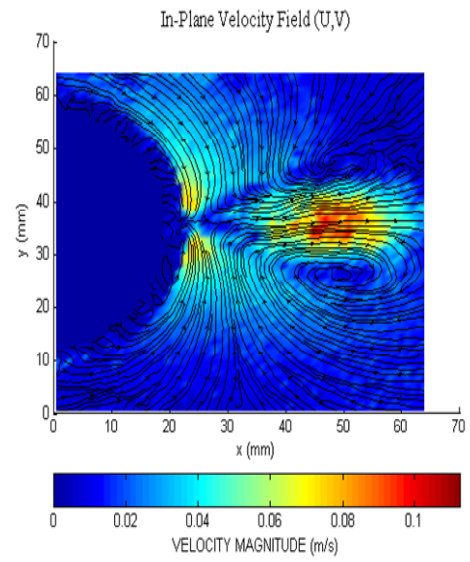
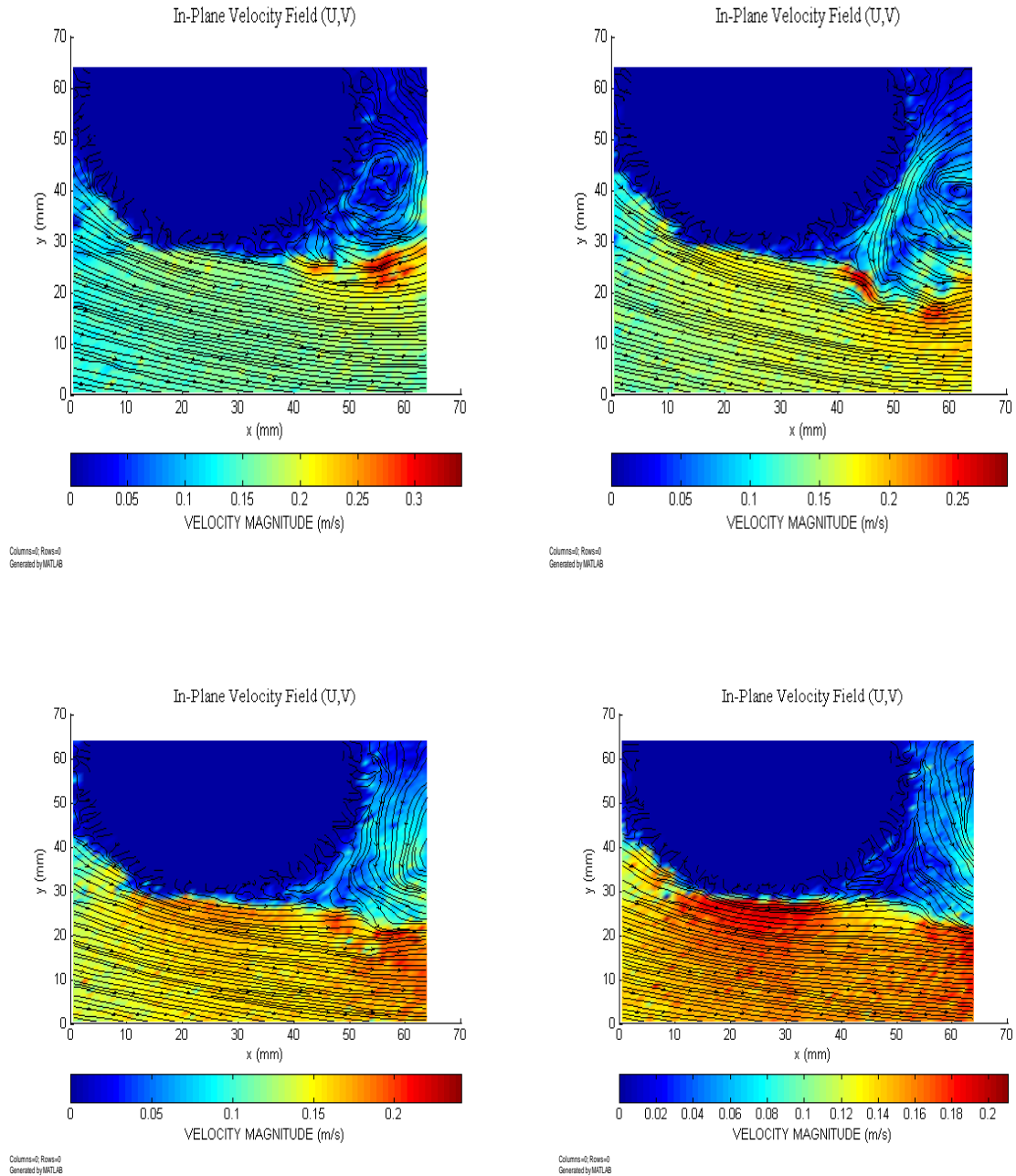


Figure 58 Average Velocity at 3.5 Hz

A2. Case 2 Synthetic Jet Cycle

Figure 59 shows 1 cycle of the synthetic jet operating at 1 Hz. The figures progress from the ejection stage in top left to the suction phase on page 68.



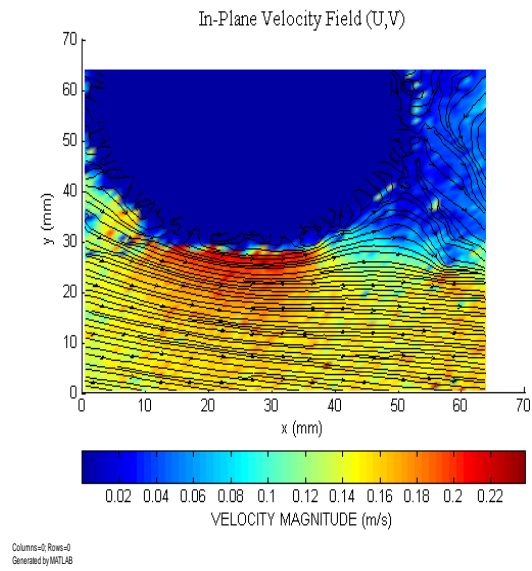


Figure 59 Stages Synthetic Jet Cycle for Case 2

Appendix B. Matlab Code used to determine Synthetic Jet Parameters and Sample Calculations

Matlab Code

```
%Scotch Yoke Equations

clear all

close all

clc

R2=.0135; % meters center of peg to mounting disk

f=3.5; %hertz

T=1/f; %Period of oscillating piston

omega=2*pi*f; %angular velocity (rads/sec)

time=[0:.01:10];

phi=pi;

theta=omega*time;

r1=R2*cos(theta+phi); %position of piston

maxr1=max(r1)

minr1=min(r1)

r1dot=R2*omega*sin(theta); %Velocity of piston

nr1dot=norm(r1dot);

lr1dot=length(r1dot);

rms=nr1dot/sqrt(lr1dot)

%Piston displacement

pistondiameter=0.0254; %meters
```

```

pistonarea=pi*(pistondiameter/2)^2;

volumedisp=pistonarea*(r1-min(r1));

totalvolumeout=pistonarea*(max(r1)-min(r1));

totalvolumein=pistonarea*(min(r1)-max(r1));

volflowrate=r1dot.*pistonarea;

% Velocity in tubing

dtub=0.0127; %meters inner diameter of tygon tubing

rtub=dtub/2; %inner radius of tygon tubing

Atub=pi*rtub^2; %Inner area of tygon tubing

Vtub=volflowrate/Atub;

%Flow out of jet

jetwidth=.00159; %meters

jetlength=0.083; %meters

jetarea=jetwidth*jetlength;

jetvelocity=(volflowrate/jetarea);

nveljet=norm(jetvelocity);

lveljet=length(jetvelocity);

rmsveljet=nveljet./sqrt(lveljet)

maxjetv=max(jetvelocity)

Tempwater=20; %deg C

nu=1.002e-3; %kinematic viscosity

rho=998.2; %Density of water

Uinf=0.114; %free stream velocity

```

Diameter=0.051; %Cylinder diameter

Re=(rho*Uinf*Diameter)/nu

St=0.20; % Assume St is 0.2 based on White Viscous Fluid Flow

sheddingf=Uinf*St/Diameter %Shedding Frequency

Cmu=2*(jetwidth/Diameter)*(rmsveljet/Uinf)^2 %Oscillatory momentum

blowing coefficient

VR=rmsveljet/Uinf % Velocity Ratio

Fplus=(f*Diameter)/Uinf

F=f/sheddingf

Sample Calculations

Reynolds Number

$$Re_D = \frac{\rho U_\infty D}{\mu}$$

$$\rho = 998.2 \frac{\text{kg}}{\text{m}^3}$$

$$U_\infty = 0.114 \frac{\text{m}}{\text{s}}$$

$$D = 0.051\text{m}$$

$$\mu = 1.002 \times 10^{-3} \frac{\text{N} \cdot \text{s}}{\text{m}^2}$$

$$Re_D = \frac{998.2 \frac{\text{kg}}{\text{m}^3} \times 0.114 \frac{\text{m}}{\text{s}} \times 0.051\text{m}}{1.002 \times 10^{-3} \frac{\text{N} \cdot \text{s}}{\text{m}^2}} = 5791.95$$

Shedding Frequency

$$f_s = \frac{St \times U_\infty}{D}$$

$$St = 0.2$$

$$D = 0.051\text{m}$$

$$U_\infty = 0.114 \frac{\text{m}}{\text{s}}$$

$$f_s = \frac{0.2 \times 0.114 \frac{\text{m}}{\text{s}}}{0.051\text{m}} = 0.45\text{Hz}$$

Dimensionless Excitation Frequency

$$F^+ = \frac{fD}{U_\infty}$$

$$f = 2.5 \frac{1}{\text{s}}$$

$$D = 0.051\text{m}$$

$$U_\infty = 0.114 \frac{\text{m}}{\text{s}}$$

$$F^+ = \frac{2.5 \frac{1}{\text{s}} \times 0.051\text{m}}{0.114 \frac{\text{m}}{\text{s}}} = 1.12$$

Velocity Ratio

$$VR = \frac{u_{\text{jrms}}}{U_\infty}$$

$$u_{\text{jrms}} = 0.58 \frac{\text{m}}{\text{s}}$$

$$U_\infty = 0.114 \frac{\text{m}}{\text{s}}$$

$$VR = \frac{0.58 \frac{\text{m}}{\text{s}}}{0.114 \frac{\text{m}}{\text{s}}} = 5.07$$

Oscillatory Momentum Blowing Coefficient

$$c_{\mu_{jrms}} = 2 \frac{h}{D} \left(\frac{u_{jrms}}{U_{\infty}} \right)^2$$

$$h = 0.00159\text{m}$$

$$D = 0.051\text{m}$$

$$u_{jrms} = 0.58 \frac{\text{m}}{\text{s}}$$

$$U_{\infty} = 0.114 \frac{\text{m}}{\text{s}}$$

$$c_{\mu_{jrms}} = 2 \frac{0.00159\text{m}}{0.051\text{m}} \left(\frac{0.58 \frac{\text{m}}{\text{s}}}{0.114 \frac{\text{m}}{\text{s}}} \right)^2 = 1.61$$

Frequency Ratio

$$F = \frac{f}{f_s}$$

$$f = 2.5 \frac{1}{\text{s}}$$

$$f_s = 0.45 \frac{1}{\text{s}}$$

$$F = \frac{2.5 \frac{1}{\text{s}}}{0.45 \frac{1}{\text{s}}} = 5.56$$

Momentum Deficit of Wake

The momentum thickness was found using:

$$\theta_{wake} = \sum_y \frac{\Delta u}{U_{\infty}} \left(1 - \frac{\Delta u}{U_{\infty}} \right),$$

where the sum was over every data point collected. The sum over all points was equivalent to the integral from $-\infty$ to ∞ .

Appendix C. Velocity Profiles

C1 Velocity Profiles at $\frac{3}{4}$ Diameter with Constant Position and Varying C_{mu}

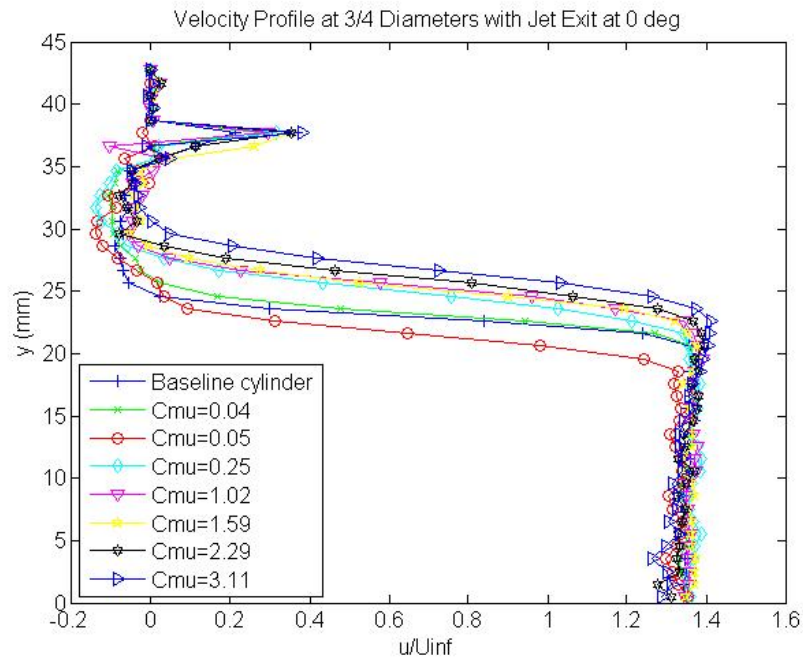


Figure 60 Velocity Profile at $\frac{3}{4}$ Diameter with Jet Exit at 0 deg and Varying C_{mu}

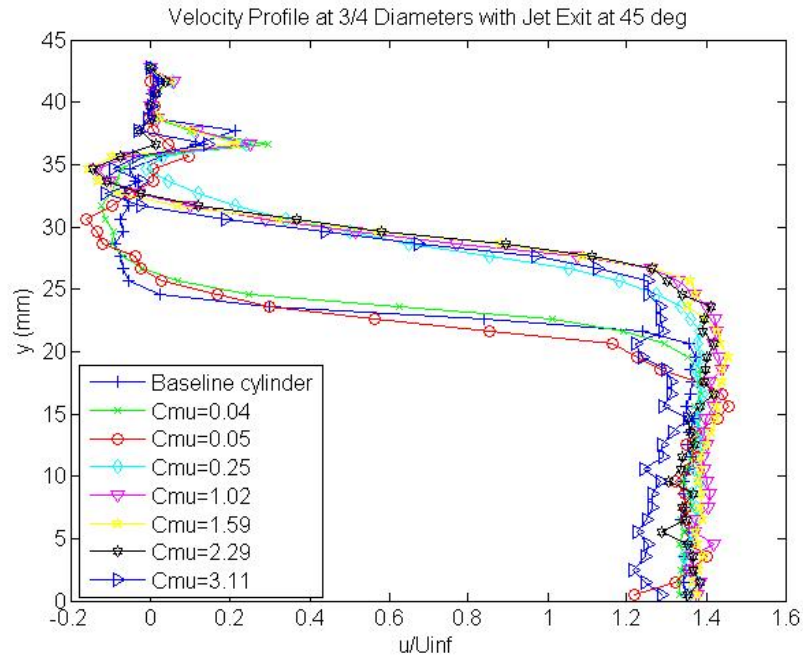


Figure 61 Velocity Profile at $\frac{3}{4}$ Diameter with Jet Exit at 45 deg and Varying C_{mu}

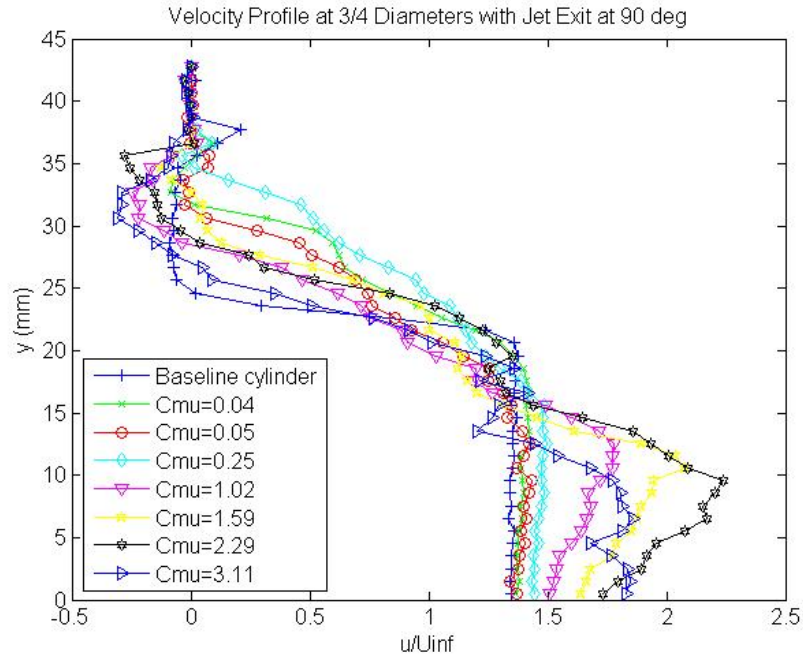


Figure 62 Velocity Profile at $\frac{3}{4}$ Diameter with Jet Exit at 90 deg and Varying C_{mu}

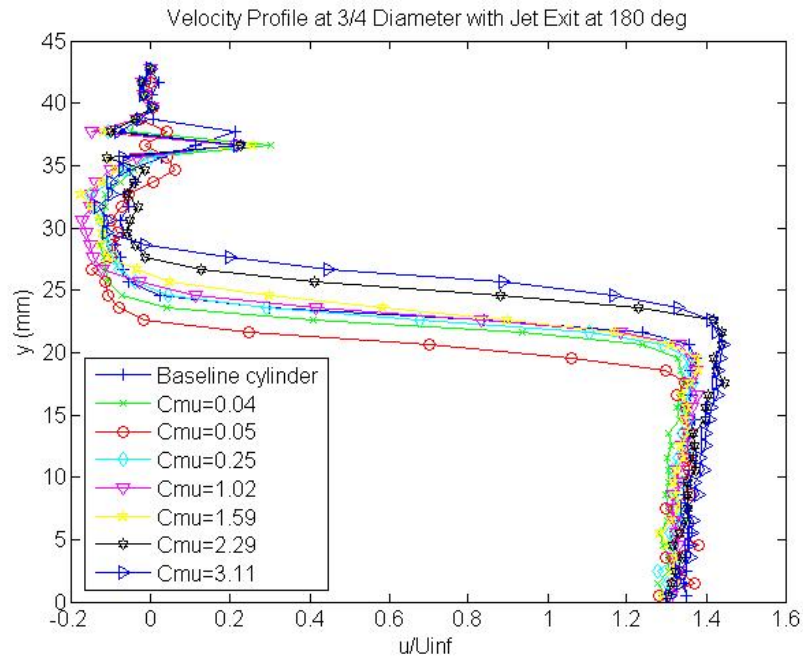


Figure 63 Velocity Profile at $\frac{3}{4}$ Diameter with Jet Exit at 180 deg and Varying C_{mu}

C2 Velocity Profiles at $\frac{3}{4}$ Diameter with Constant C_{mu} and Varying Jet Location

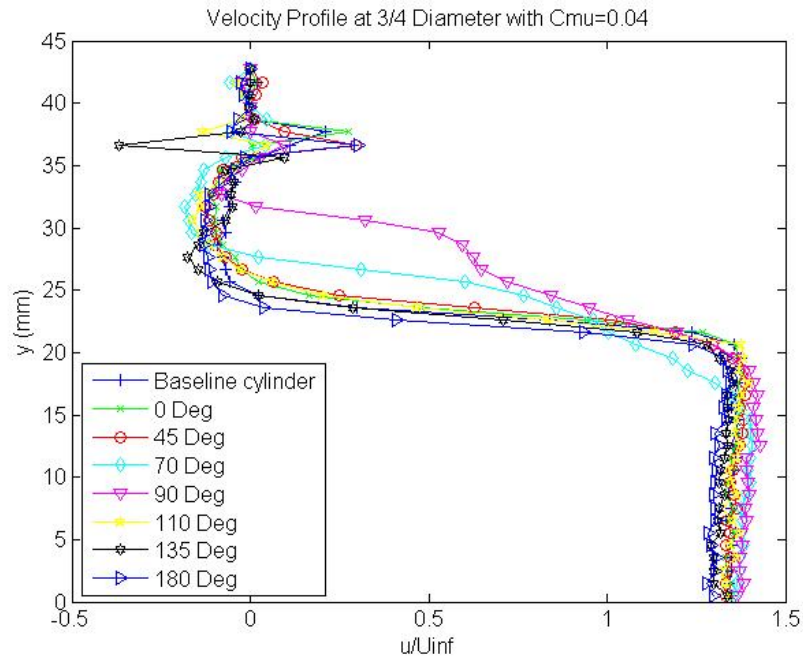


Figure 64 Velocity Profile at $\frac{3}{4}$ Diameter with $C_{mu}=0.04$ and Varying Jet Location

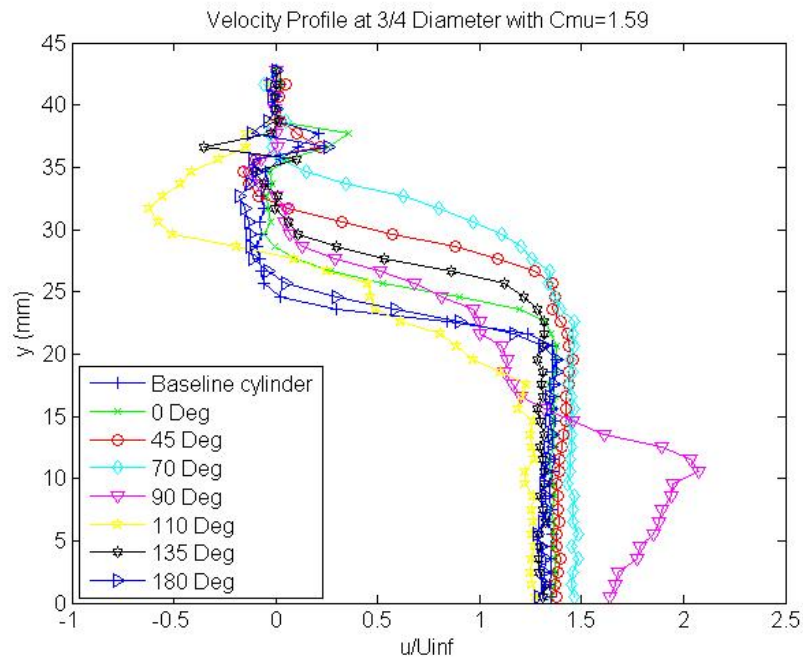


Figure 65 Velocity Profile at $\frac{3}{4}$ Diameter with $C_{mu}=1.59$ and Varying Jet Location

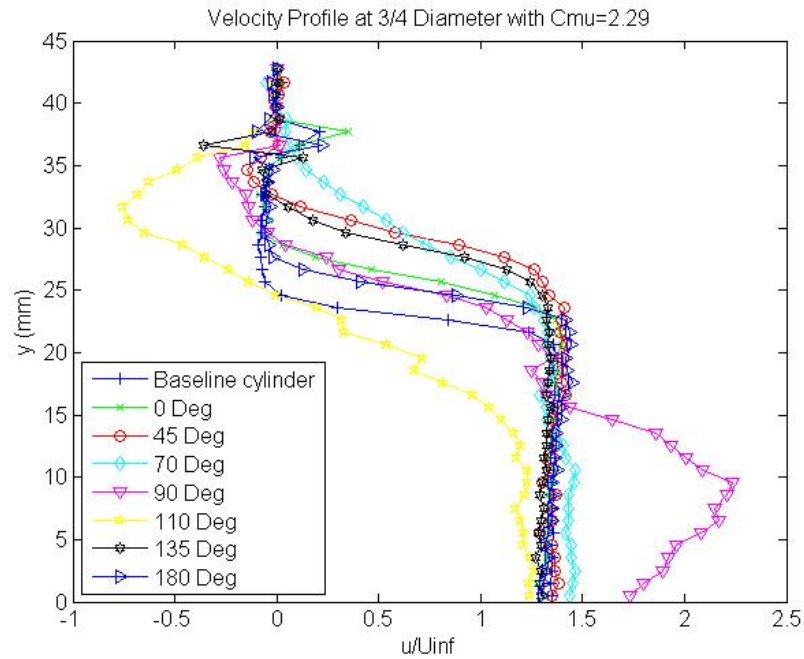


Figure 66 Velocity Profile at $\frac{3}{4}$ Diameter with $C_{mu}=2.29$ and Varying Jet Location

C2 Velocity Profiles Aft of the Cylinder

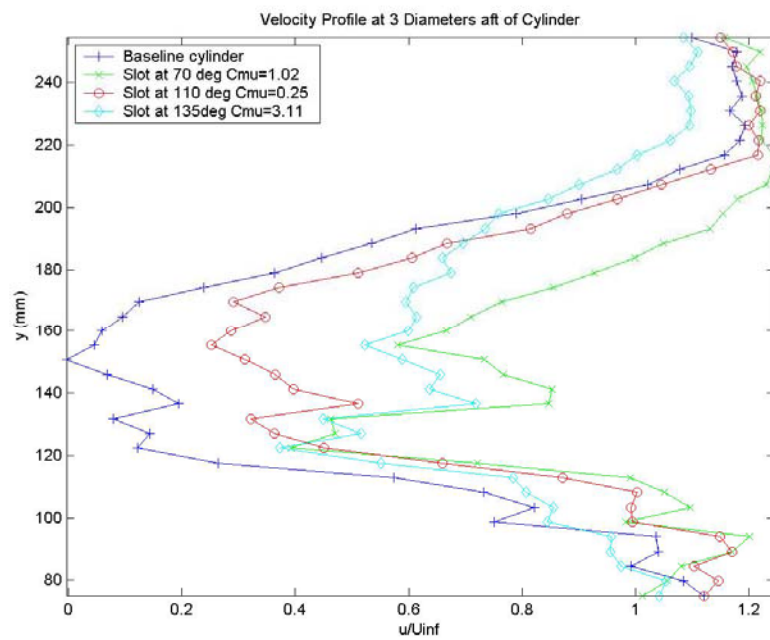


Figure 67 Velocity Profile at 3 Diameters Aft of Cylinder

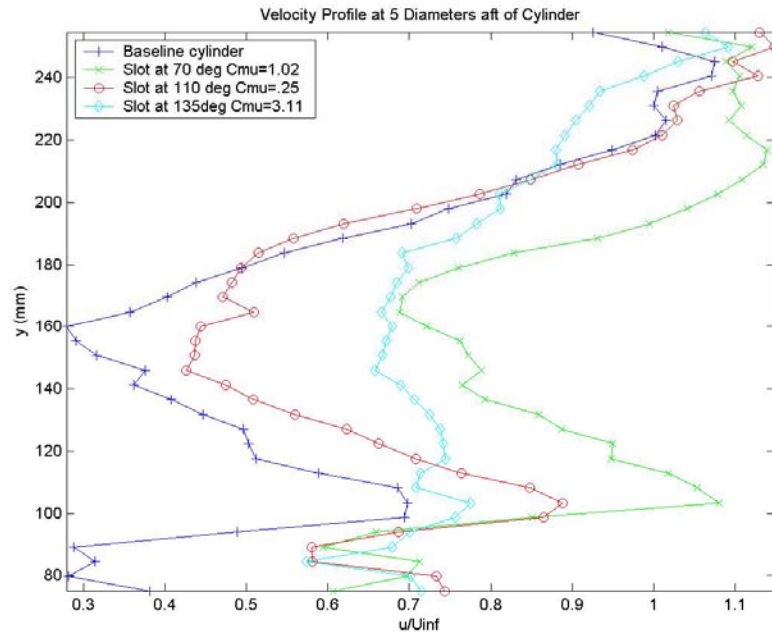


Figure 68 Velocity Profile at 5 Diameters Aft of Cylinder

Bibliography

1. Amitay, Michael, Andrew Honohan, Mark Trautman and Ari Glezer, "Modification of the Aerodynamic Characteristics of Bluff Bodies Using Fluidic Actuators." AIAA Paper No. 97-2004.
2. Amitay, Michael, Barton L. Smith and Ari Glezer, "Aerodynamic Flow Control using Synthetic jet Technology." 36th Aerospace Sciences Meeting and Exhibit, Reno, NV, Jan 1998. AIAA Paper No. 98-0208.
3. Bera, Jean-Christophe and Michel Sunyach. "Control of Boundary layer Separation by Jet Oscillation." 4th AIAA/CEAS Aeroacoustics Conf., Toulouse, France, June 98. AIAA Paper No. 98-2373.
4. "Boundary Layers." University of Leeds. 20 January 2005
http://www.efm.leeds.ac.uk/CIVE/CIVE1400/Section4/boundary_layer.htm.
5. Flow Manager software and Introduction to PIV Instrumentation: Software user's Guide. Dantec Dynamics. Skovlunde, Denmark, 2000.
6. Glezer, Ari and Michael Amitay. "Synthetic Jets." Annual Review of Fluid Mechanics. 2002,34:1-36.
7. Honohan, Andrew M., Michael Amitay and Ari Glezer, "Aerodynamic Control Using Synthetic Jets." FLUIDS 2000 Conference and Exhibit, Denver, CO, June 2000. AIAA Paper No. 2000-2401.
8. Incropera, Frank P. and David P. DeWitt. Fundamentals of Heat and Mass Transfer (Fourth Edition). New York: John Wiley and Sons, 1996.
9. MD-2 Dual Stepper Motor System User's Guide. Arrick Robotics. Texas, 1995.
10. Naim, A., D. Greenblatt, A. Seifert and I. Wagnanski, "Active Control of Cylinder Flow with and without a Splitter Plate using Piezoelectric Actuators." 1st Flow Control Conference, St. Louis, MO, June 2002. AIAA Paper No. 2002-3070
11. Rao, P., J. L. Gilarranz, J. Ko, T. Strganac and O. K. Rediniotis., "Flow Separation Control Via Synthetic Jet Actuation." 38th AIAA Aerospace Sciences meeting and Exhibit, Reno, NV, January 2000. AIAA Paper No. 2000-0407.
12. "The Scotch-Yoke." Dynamics. University of Florida. 13 March 2005
<https://aemes.mae.ufl.edu/~uhk/DYNAMICS.html>.

13. Shih, Chiang. "Turbulent Wake Behind a Circular Cylinder." Flow Over a Circular Cylinder. Florida State University. 24 October 2004
<http://www.eng.fsu.edu/~shih/succeed/cylinder/cylinder.htm>.
14. Smith, Barton L. and Ari Glezer, "The formation and evolution of synthetic Jets." *Physics of Fluids* Vol 10, Number 9 2281.
15. Tomar, S., J. Arnaud and J. Soria, "Structure of a Zero-net-mass-flux round jet in crossflow." 15th Australian Fluid Mechanics Conference, Sydney, Australia, December 2004. AFMC00224.
16. Tuck, A. and J. Soria, "Active Flow Control over a NACA 0015 Airfoil using a ZNMF Jet." 15th Australian Fluid Mechanics Conference, Sydney, Australia, December 2004. AFMC00178.
17. University Desktop Water Tunnel Model 0710: Tunnel and Experiment Overview. Rolling Hills Research Corporation, El Segundo, Ca.
18. White, Frank M. Viscous Fluid Flow. (Second Edition) Massachusetts: McGraw Hill, 1991.
19. Yehoshua, Tal and Avi Seifert, "Boundary Condition Effects on Oscillatory Momentum Generators." 33rd AIAA Fluid Dynamics Conference and Exhibit, Orlando, FL, June 2003. AIAA Paper No. 2003-3710.

Vita

Captain Christopher K. Smith graduated from Centennial High School, Peoria, AZ in June 1996. He entered college at Arizona State University, Tempe, Arizona where he graduated with a Bachelor of Science degree in Mechanical Engineering. He was commissioned as a Second Lieutenant in the United States Air Force through AFROTC Detachment 025 at Arizona State University in May 2000.

His first assignment was to Air to Air Missile Test Flight, Munitions Test Division, 46th Test Wing, Eglin Air Force Base, FL. While there he served as an Air Supremacy Systems Test Engineer. In August 2003, he entered the Graduate School of Engineering and Management, Air Force Institute of Technology to pursue a Master's of Science in Aeronautical Engineering. Upon graduation, he will be assigned to the United States Air Force Test Pilot School to attend the Flight Test Engineer Course as part of TPS Class 05B.

| REPORT DOCUMENTATION PAGE | | | | Form Approved OMB No. 074-0188 | |
|--|---------------|-----------------------------------|--|--|--|
| <p>The public reporting burden for this collection of information is estimated to average 1 hour per response, including the time for reviewing instructions, searching existing data sources, gathering and maintaining the data needed, and completing and reviewing the collection of information. Send comments regarding this burden estimate or any other aspect of the collection of information, including suggestions for reducing this burden to Department of Defense, Washington Headquarters Services, Directorate for Information Operations and Reports (0704-0188), 1215 Jefferson Davis Highway, Suite 1204, Arlington, VA 22202-4302. Respondents should be aware that notwithstanding any other provision of law, no person shall be subject to a penalty for failing to comply with a collection of information if it does not display a currently valid OMB control number.</p> <p>PLEASE DO NOT RETURN YOUR FORM TO THE ABOVE ADDRESS.</p> | | | | | |
| 1. REPORT DATE (DD-MM-YYYY) 13-06-2005 | | 2. REPORT TYPE Master's Thesis | | 3. DATES COVERED (From – To) September 2003 – June 2005 | |
| 4. TITLE AND SUBTITLE Boundary Layer Control of a Circular Cylinder Using a Synthetic Jet | | | | 5a. CONTRACT NUMBER | |
| | | | | 5b. GRANT NUMBER | |
| | | | | 5c. PROGRAM ELEMENT NUMBER | |
| 6. AUTHOR(S) Smith, Christopher K., Capt, USAF | | | | 5d. PROJECT NUMBER | |
| | | | | 5e. TASK NUMBER | |
| | | | | 5f. WORK UNIT NUMBER | |
| 7. PERFORMING ORGANIZATION NAMES(S) AND ADDRESS(S) Air Force Institute of Technology Graduate School of Engineering and Management (AFIT/EN) 2950 Hobson Way WPAFB OH 45433-7765 | | | | 8. PERFORMING ORGANIZATION REPORT NUMBER AFIT/GAE/ENY/05-J12 | |
| 9. SPONSORING/MONITORING AGENCY NAME(S) AND ADDRESS(ES) N/A | | | | 10. SPONSOR/MONITOR'S ACRONYM(S) | |
| | | | | 11. SPONSOR/MONITOR'S REPORT NUMBER(S) | |
| 12. DISTRIBUTION/AVAILABILITY STATEMENT APPROVED FOR PUBLIC RELEASE; DISTRIBUTION UNLIMITED. | | | | | |
| 13. SUPPLEMENTARY NOTES | | | | | |
| 14. ABSTRACT Active control of flow around a circular cylinder at a sub-critical Reynolds number was studied experimentally. The flow was controlled by using a synthetic jet which ran span wise along the cylinder and emanated radially from the cylinder. The experiments were conducted over a two dimensional cylinder in a water tunnel at a Reynolds number of approximately 5800. Seven different jet locations and seven different jet oscillation frequencies were examined. Particle image velocimetry (PIV) was used for flow visualization. The synthetic jet proved to delay flow separation at a wide range of locations and oscillation frequencies. The greatest positive effect on the boundary layer was determined to be when the jet was placed at an angle of 70° to the on coming flow at an oscillatory momentum blowing coefficient at 1.03, and non-dimensional frequency of 0.9. Boundary layer separation was delayed from approximately 90° to approximately 140° and the momentum deficit was reduced by 77-88%. | | | | | |
| 15. SUBJECT TERMS Synthetic Jet, Flow Control, Boundary Layer Control, Laminar Boundary Layer, Boundary Layer Transition, Particle Image Velocimetry , Flow Visualization, Circular Cylinder, Water Tunnel | | | | | |
| 16. SECURITY CLASSIFICATION OF: | | 17. LIMITATION OF ABSTRACT | | 18. NUMBER OF PAGES 97 | |
| REPORT U | ABSTRACT U | | | | |
| | | | | 19a. NAME OF RESPONSIBLE PERSON Milotn E. Franke, PhD, AFIT/ENY | |
| | | | | 19b. TELEPHONE NUMBER (Include area code) (937) 255-3636, ext 4720 | |